

Article

Performance of a Rotating Detonation Rocket Engine with Various Convergent Nozzles and Chamber Lengths

John W. Bennowitz ^{1,*} , Blaine R. Bigler ², Mathias C. Ross ³, Stephen A. Danczyk ¹, William A. Hargus Jr. ¹ 
and Richard D. Smith ⁴

¹ Air Force Research Laboratory, Edwards, CA 93524, USA; stephen.danczyk@us.af.mil (S.A.D.); william.hargus@us.af.mil (W.A.H.J.)

² Jacobs Technology Group, Air Force Research Laboratory, Edwards, CA 93524, USA; blaine.bigler.ctr@us.af.mil

³ Department of Mechanical and Aerospace Engineering, UCLA, Los Angeles, CA 90095, USA; mathias.ross.ctr@us.af.mil

⁴ GHKN Engineering LLC., Kirkland, WA 98034, USA; rick@doylesmith.com

* Correspondence: john.bennowitz.1@us.af.mil

Abstract: A rotating detonation rocket engine (RDRE) with various convergent nozzles and chamber lengths is investigated. Three hundred hot-fire tests are performed using methane and oxygen ranging from equivalence ratio equaling 0.5–2.5 and total propellant flow up to 0.680 kg/s. For the full-length (76.2 mm) chamber study, three nozzles at contraction ratios $\epsilon_c = 1.23, 1.62$ and 2.40 are tested. Detonation is exhibited for each geometry at equivalent conditions, with only fuel-rich operability slightly increased for the $\epsilon_c = 1.62$ and 2.40 nozzles. Despite this, counter-propagation, i.e., opposing wave sets, becomes prevalent with increasing constriction. This is accompanied by higher number of waves, lower wave speed U_{wv} and higher unsteadiness. Therefore, the most constricted nozzle always has the lowest U_{wv} . In contrast, engine performance increases with constriction, where thrust and specific impulse linearly increase with ϵ_c for equivalent conditions, with a 27% maximum increase. Additionally, two half-length (38.1 mm) chambers are studied including a straight chamber and $\epsilon_c = 2.40$ nozzle; these shortened geometries show equal performance to their longer equivalent. Furthermore, the existence of counter-propagation is minimized. Accompanying high-fidelity simulations and injection recovery analyses describe underlying injection physics driving chamber wave dynamics, suggesting the physical throat/injector interaction influences counter-propagation.

Keywords: rotating detonation rocket engine; detonation; counter-propagation; wave dynamics; injection recovery



Citation: Bennowitz, J.W.; Bigler, B.R.; Ross, M.C.; Danczyk, S.A.; Hargus, W.A.; Smith, R.D. Performance of a Rotating Detonation Rocket Engine with Various Convergent Nozzles and Chamber Lengths. *Energies* **2021**, *14*, 2037. <https://doi.org/10.3390/en14082037>

Academic Editor: Vijay Anand

Received: 11 February 2021

Accepted: 1 April 2021

Published: 7 April 2021

Publisher's Note: MDPI stays neutral with regard to jurisdictional claims in published maps and institutional affiliations.



Copyright: © 2021 by the authors. Licensee MDPI, Basel, Switzerland. This article is an open access article distributed under the terms and conditions of the Creative Commons Attribution (CC BY) license (<https://creativecommons.org/licenses/by/4.0/>).

1. Introduction

Rotating detonation engines (RDEs) have recently gained substantial interest as an alternative to traditional deflagration-based propulsion systems, with the theoretical potential to achieve overall engine performance gains. Specifically, rotating detonation rocket engines (RDREs) can exhibit an increase in chamber pressure, temperature and exhaust gas velocity for a substantially lower injection pressure through a constant-volume combustion process, compared to constant-pressure devices. Recent studies have demonstrated the successful operation of RDREs using both gaseous [1–7] and liquid fuels [1,8]. However, insight into the optimal method to properly expand the highly unsteady exhaust flow from the RDRE is still limited, as reflected waves back upstream from a physical throat constriction can interact with the reactant fill region to disrupt the detonation zone [9].

To date, only limited experimental studies with convergent throats have been performed for RDEs, with detonative behavior ranging from increased complexity of the detonation mode structure [2,5,10,11] to a complete detonative breakdown to deflagration

processes [12]. Therefore, to further understand the flow expansion processes associated with a rotating detonation engine, a detailed study using multiple convergent throat geometries is conducted in the current study. First, in addition to the straight annulus exit ($\epsilon_c = 1.00$), three physical throat designs are considered for the full annular length geometry ($l_c = 76.2$ mm, $W_c = 5$ mm) that correspond to contraction ratios $\epsilon_c = 1.23$, 1.62, and 2.40. A linear performance increase is observed for a given physical throat up to 1335 N thrust at 0.680 kg/s total propellant mass flow, which is also accompanied by an increase in the prevalence of counter-propagating modal behavior. For example, the most constricted annular geometry exhibits counter-propagating behavior across all of the flow conditions investigated. This is contrary to traditional design guidelines for RDEs, as counter-propagating behavior, i.e., two opposing sets of waves moving in opposite directions, is associated with lower wave speeds and a decrease in performance due to a likely increase in parasitic deflagration [5]. In addition, a series of tests have been conducted using two half annular length configurations ($l_c = 38.1$ mm) including a straight annulus and the most constricted $\epsilon_c = 2.40$ nozzle. Notably, engine performance is the same for the shortened straight $\epsilon_c = 1.00$ geometry compared to the full-length annulus, and the shortened annulus with the $\epsilon_c = 2.40$ nozzle yields approximately 6% higher performance. Furthermore, the detonation wave speeds are typically up to 5% faster for the shortened straight annular geometry compared to the longer configuration at the same flow condition. For the shortened $\epsilon_c = 2.40$ nozzle, detonation mode structure is significantly better ordered compared to the full-length geometry, i.e., the existence of counter-propagating behavior is significantly diminished. This result is consistent with the theory proposed herein that shock waves reflected back upstream from the annular throat can influence the quality of reactant mixedness, and thus the detonation mode structure, in the reactant fill region near the injector face. A supporting analysis describing the injector recovery process and accompanying results from high-fidelity simulations of the RDRE are also detailed in this manuscript. These analyses suggest the interaction between the observed injection response and interaction with a physical throat is one driving mechanism responsible for counter-propagating modal behavior. The results of this work should serve as a basis for further studies to optimize RDRE annular nozzle design, as well as global engine performance.

2. Experiment Setup

The modular RDRE tested in this study is the same laboratory engine used in our previous work [5,13,14]. It was originally designed and tested by Smith and Stanley [2,15] using empirical guidelines developed by Bykovskii et al. [1], and contains a 76.2 mm diameter annulus with a 5 mm annular width, and a 76.2 mm long annular channel (see Figure 1). Gaseous propellants, methane GCH_4 and oxygen GO_2 , are fed through 72 opposing fuel and oxidizer jets equally distributed around the annulus in an unlike impinging injector configuration. The baseline injector used in the previous study had a very high injector initial pressure drop across the investigated flow conditions [5]. Therefore to reduce the required drive pressures, the injector used in the present study contains larger sized holes for both the fuel and oxidizer equivalent in both cases to $1.5\times$ the original baseline injection areas.

Propellant flow rates are metered using critical flow venturis, with total mass flow rates ranging up to 0.680 kg/s. For the flow conditions investigated, fuel and oxidizer manifold pressures are high enough to cause the injector flow to be choked whenever a detonation wave is not located directly over a specific injection site. A pre-detonator tube using GCH_4 and GO_2 , and firing tangentially into the annulus near the injector face is used for ignition. A planar detonation wave is generated in the pre-detonator tube from a small volume (53 cm^3) of premixed gas located in an upstream reservoir that is ignited using a spark plug.

Equivalent chamber pressure for the annulus of the rotating detonation rocket engine is measured through two capillary tube attenuated pressure (CTAP) static probes, the ports

for which are located at 8.89 mm and 29.21 mm axially downstream from the injector face. The CTAP dimension, i.e., l/d ratio, is based on the work of Stevens et al. [16], and is high enough to filter the oscillatory pressure to provide an equivalent average chamber pressure. Three high-frequency pressure transducers are also used to measure pressure fluctuations within each plenum (2 ea.) and within the main chamber (1 ea.). The plenum pressure transducers are both PCB model 112A05 and are used to assess the degree of detonation-plenum coupling. The chamber sensor is a PCB model 123A, which uses both water-cooling and a helium bleed on its surface to increase survivability. This chamber sensor is flush mounted at the same axial position as the second CTAP sensor. All high-frequency pressure sensors are sampled at 500 kHz. Thrust measurements are also taken for each firing using a thrust stand with a 1112 N load cell. The RDRE test article on the thrust stand, as well as a side-view during a typical firing can be seen in Figure 1a,b.

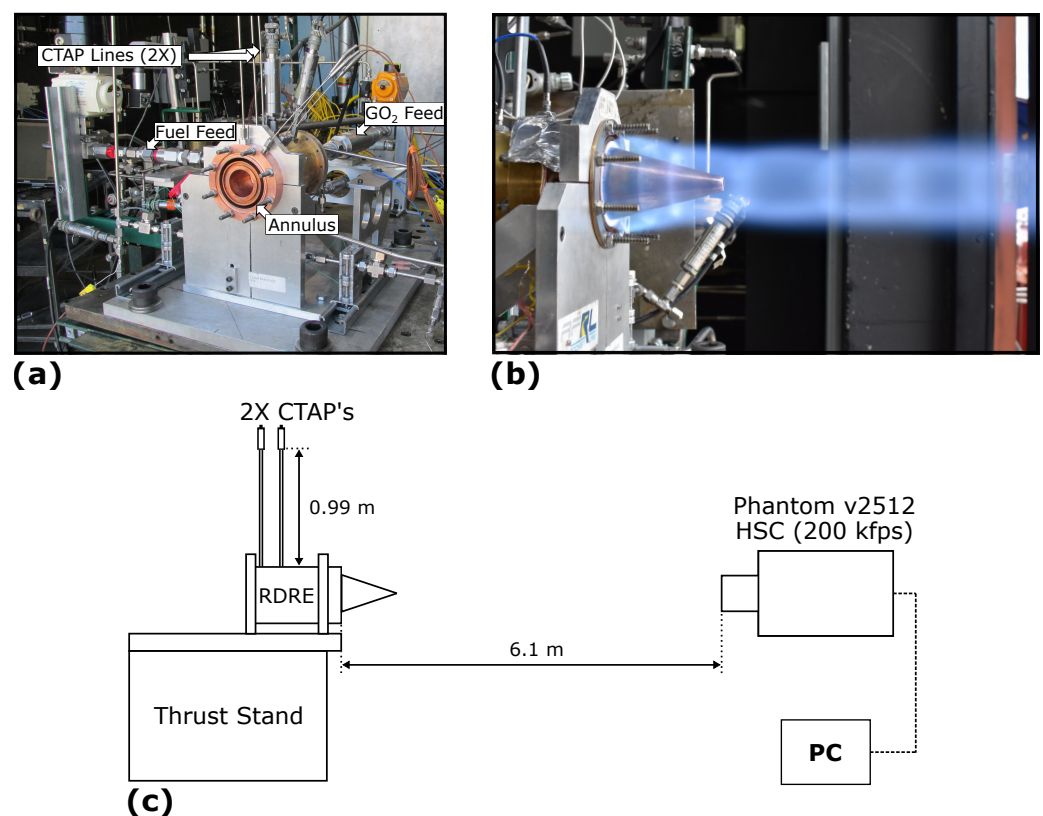


Figure 1. Depiction of the RDRE mounted on the thrust stand (a) before a test (labeled isometric view), (b) during a test firing (side view), and (c) schematic view of the experimental apparatus with high-speed camera configuration.

Direct high-speed visible imaging into the annulus is used to observe and capture the traveling detonation waves. The high-speed camera (HSC) is a Phantom v2512 positioned 6.1 m downstream of the test article (see Figure 1c). The camera is located within a protective enclosure with a quartz window and is focused on the injection plane close to the detonation zone. A Nikon Reflex-Nikkor HN-27 lens is used in conjunction with the camera to allow the RDRE annulus to fill the entire image field-of-view. Images are captured at 200 kfps with a resolution of 256×256 pixels and exposure times between 1 and 3 μ s.

Convergent Nozzle Geometries

In order to investigate the effects of various convergent nozzles for the full annular 76.2 mm length configuration, four geometries of varying contraction ratio ϵ_c are tested: (1) straight annulus ($\epsilon_c = 1.00$), (2) $\epsilon_c = 1.23$, (3) $\epsilon_c = 1.62$, and (4) $\epsilon_c = 2.40$. These four

geometries correspond to annular constriction widths of 5 mm, 3.98 mm, 3.00 mm and 2.01 mm, respectively. For each of these tests, a 15 degree conical spike is added to the end of the annular geometry to help with the effective expansion of the supersonic exhaust gases. In order to avoid flow separation at the exit interface of the annulus, the nozzle throat location is effectively moved upstream with increasing contraction ratio to maintain a 15 degree contour into the conical spike (see Figure 2a). This causes the center body of the RDRE to be modular in design with various physical throat additions (Figure 2b). Similarly, two reduced annular length geometries with $l_c = 38.1$ mm are also tested: a straight center body design and one with the most constricted $\epsilon_c = 2.40$ nozzle. It should be noted during the testing of these configurations, both the outer and center bodies have the same annular length, i.e., the center body is not recessed. As with the full annular length designs, the 15 degree conical spike is added for these shorter configurations and the axial throat contour for the $\epsilon_c = 2.40$ nozzle adjusted to maintain the 15 degree expansion contour past the throat. A summary of the dimensions for the convergent nozzles and their respective throat locations are presented in Table 1.

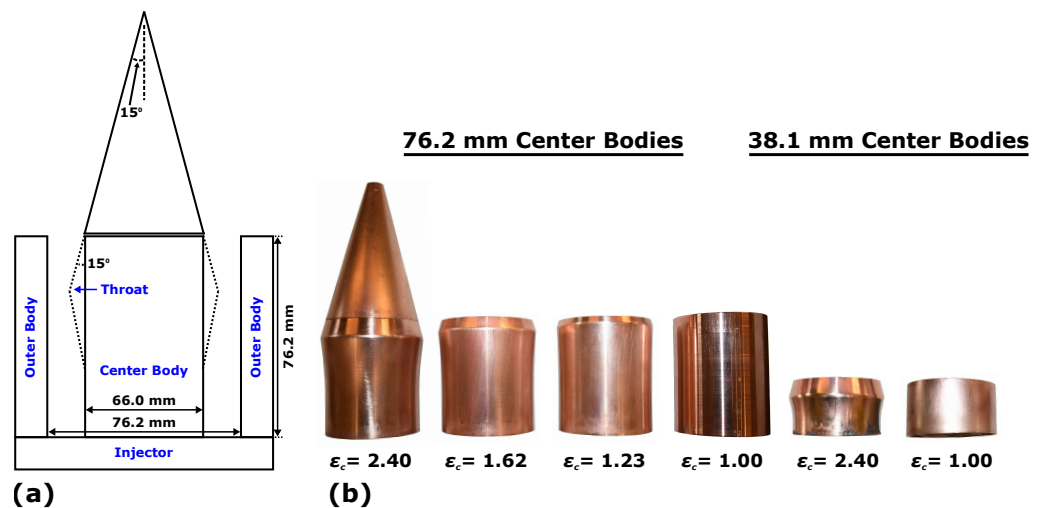


Figure 2. Various RDRE nozzle geometries including the (a) conceptual view of the modular configuration, along with the (b) tested center bodies for both the $l_c = 76.2$ mm and 38.1 mm designs.

Table 1. Relevant dimensions for the investigated convergent nozzles.

Contraction Ratio ϵ_c	Annular Length l_c (mm)	Nozzle Throat Size (mm)	Throat Axial Distance (mm)
1.23	76.2	3.98	73.9
1.62	76.2	3.00	70.4
2.40	76.2	2.01	66.6
2.40	38.1	2.01	27.2

3. Convergent Nozzle Study: Full Annular Length Geometries

For each annular configuration, three sets of flow conditions are investigated for varying equivalence ratio ϕ and total propellant mass flow \dot{m}_{tot} . The first set varies equivalence ratio ϕ from ≈ 0.5 to 2.5 in 0.2–0.25 increments, while holding the total mass flow rate of the propellants constant at 0.272 kg/s. The other two condition sets include fixing the equivalence ratio constant at both $\phi = 1.15$ and 1.5, while varying \dot{m}_{tot} from 0.2 to 0.680 kg/s. The flow condition test matrix for this study is seen in Figure 3.

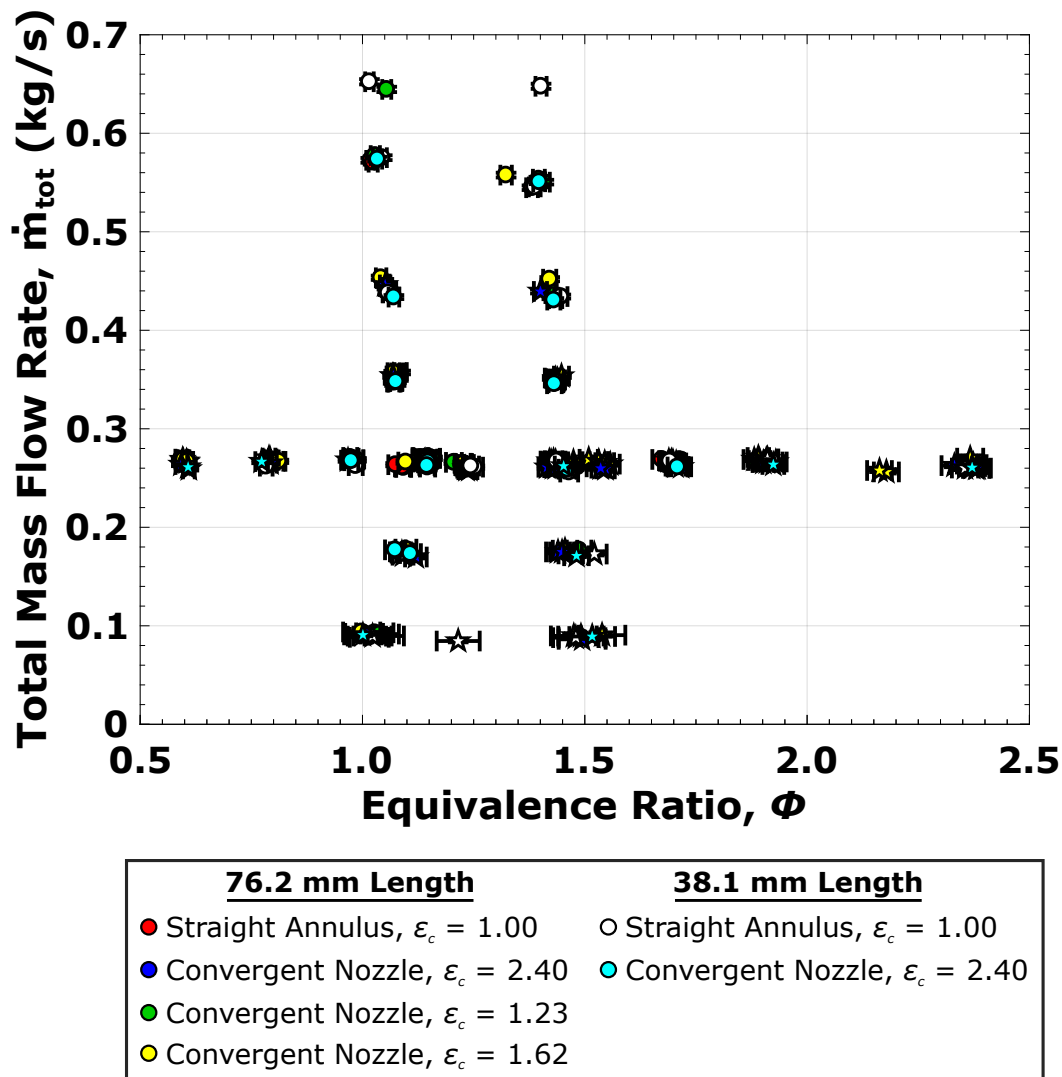


Figure 3. Flow condition test matrix for the various convergent nozzle geometries.

In the previous experimental work, hot-fire tests of the RDRE were 1250 ms in duration [5,13]. However, due to the inclusion of the temperature-sensitive high-frequency pressure transducer, the firing times for all of these tests are reduced to 750 ms to increase the survivability of the sensor. Figure 4 compares two test firings of 1250 ms and 750 ms for the same flow condition, $\phi = 1.15$ and $\dot{m}_{tot} = 0.272$ kg/s, showing the transient response of the test article pressures (left) and thrust (right) for the two firings. For both run durations, the upstream venturi and plenum pressures reach steady-state conditions throughout the entirety of the engine run time, whereas the oscillations present initially in the thrust measurement damp out during the last 100 ms of the firing. Therefore, the 100 ms duration bounded by the vertical dashed lines in Figure 4 is used for reporting the average run measurements. As the average test measurements captured during the 750 ms run are equivalent to the 1250 ms firing without significant noise added, this provides validation for the short-duration firing time. Measurement uncertainty for these reduced duration firings are calculated using the procedure described in Lightfoot et al. [17]. This uncertainty is presented as error bars on all of the subsequent test run measurement plots, which overall did not increase notably from previous extended firing results with 1250 ms run duration [5].

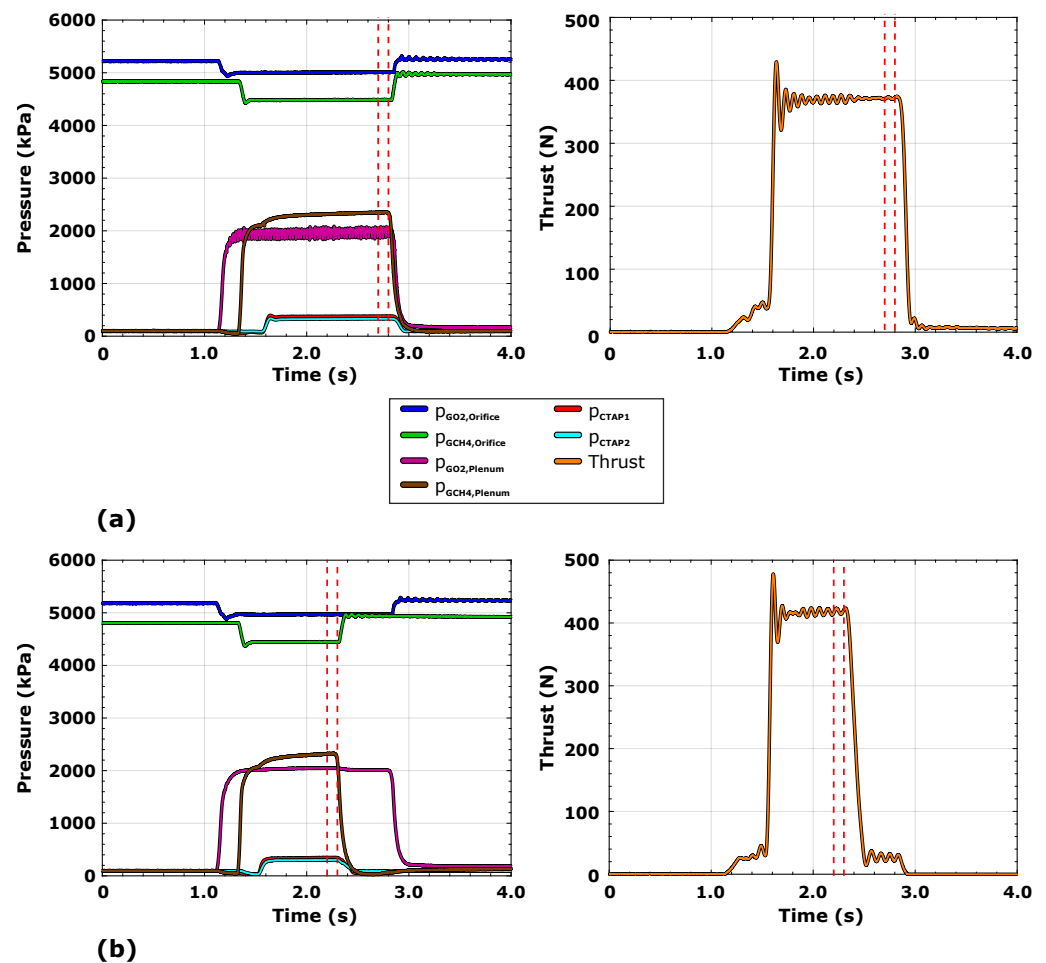


Figure 4. Example data for two tests showing both the system pressures (**left**), as well as thrust measurements (**right**) for a (a) 1250 ms and (b) 750 ms firing at the same flow condition. It should be noted that the dashed vertical lines bound the 100 ms range used for the reported average run measurements.

3.1. Engine Operability and Performance

Global performance measurements for the equivalence ratio set of flow conditions at 0.272 kg/s total flow rate are shown in Figure 5, which compare the various full $l_c = 76.2$ mm annular length convergent nozzle geometries. In general, detonation is achieved across a majority of the equivalence ratio conditions ranging from $\phi = 0.5$ to 2.0 for each convergent nozzle. From $\phi = 2.0$ to 2.5, successful operation is observed for $\epsilon_c = 1.62$ and 2.40, likely a result of modified annular flow conditions (i.e., chamber gas accumulation) conducive to engine ignition due to the physical throat addition. Maximum performance occurs from $\phi \approx 1.15$ –1.5, and this range is not altered with increasing nozzle contraction ratio. These flow conditions correspond to a maximum thrust F of 556 N and specific impulse I_s of 225 s for the most constricted $\epsilon_c = 2.40$ configuration. In addition, both performance parameters display a linear increase with increasing physical throat constriction for a specific flow condition; the $\epsilon_c = 1.23$, 1.62 and 2.40 nozzles show an overall increase of 8%, 15% and 28% from the straight annulus design, respectively. This linear relationship for these performance parameters is shown in greater detail in Figure 5c,d, where the average percent increase for thrust and specific impulse is plotted as a function of contraction ratio for the investigated equivalence ratio flow conditions. In these calculations, Chauvenet's rejection criteria [18] is implemented to remove outlying data and the Student's t -distribution for small sample size [19] is used to quantify the statistical uncertainties associated with the F and I_s percent increases. As can be seen in this figure, the uncertainty for both the F and I_s percent increases is fairly small across the varying

contraction ratio nozzles, with the $\epsilon_c = 2.40$ nozzle having the largest error of approximately $\pm 3\%$. Nevertheless, the linear trend with increasing contraction ratio for both performance parameters is clear.

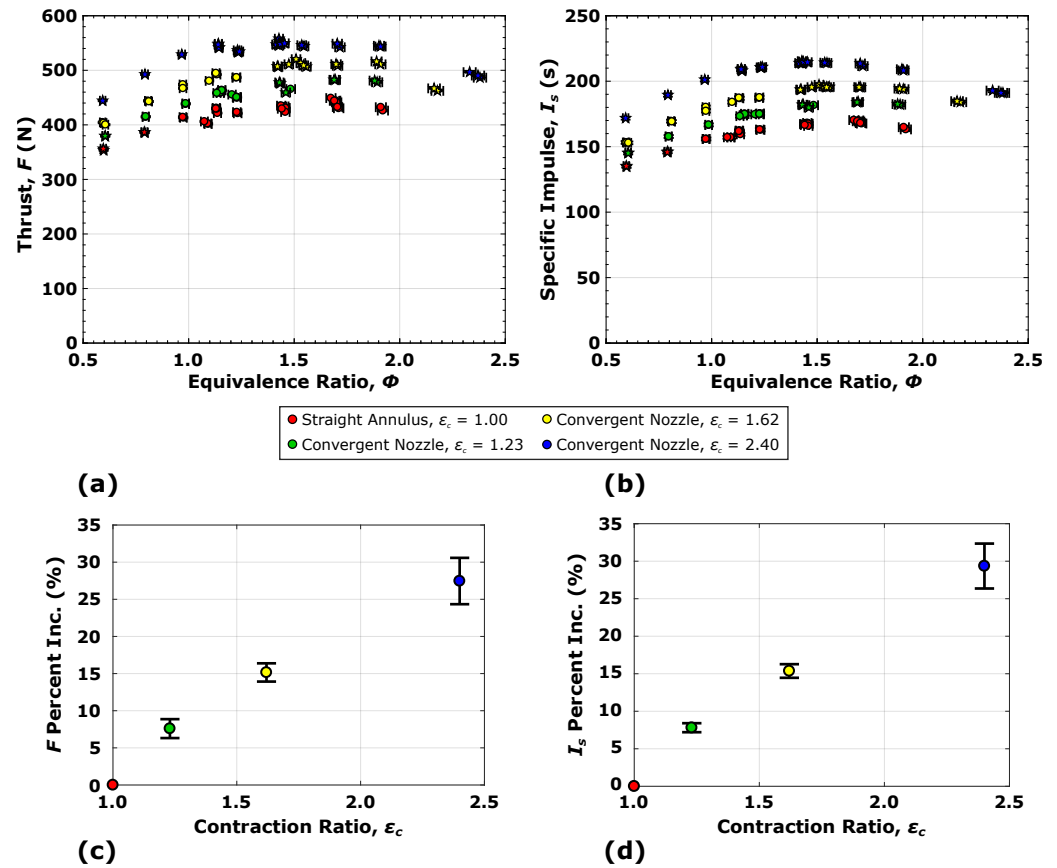


Figure 5. Performance summary for the $l_c = 76.2$ mm convergent nozzle study showing (a) thrust F and (b) specific impulse I_s for the equivalence ratio flow conditions at $\dot{m}_{tot} = 0.272$ kg/s, as well as average percent increase for (c) F and (d) I_s as a function of contraction ratio ϵ_c across these conditions. Depending on the flow condition and convergent nozzle geometry, the engine operates in either a corotating (\bullet) or counter-propagating mode (\star).

RDRE performance sensitivity to increasing total propellant flow rate for constant equivalence ratios equaling 1.15 and 1.5 is shown in Figure 6. Similarly to the runs over the range of equivalence ratios, successful detonation is achieved for the entire flow range from $\dot{m}_{tot} = 0.091$ to 0.453 kg/s across all nozzle geometries. One notable observation is that tests from 0.453 to 0.680 kg/s are only shown for the straight annulus geometry and $\epsilon_c = 1.23$. This is due to nozzle erosion occurring during tests exceeding 0.454 kg/s for the $\epsilon_c = 1.62$ and 2.40 nozzles and results are therefore omitted. Measured thrust linearly increases across the whole range for each configuration, which reaches a maximum of 1334 N for $\epsilon_c = 1.23$ at $\dot{m}_{tot} \approx 0.680$ kg/s. It should be noted that while the load cell used is rated up to 1112 N, there are a small number of tests that exceed this rating. As there is no alteration in the linear trend observed for the thrust measurements between 1110 and 1335 N, they can be considered reasonable but most likely have greater measurement uncertainty. The specific impulse rapidly increases with increasing flow rate for all geometries until 0.340 kg/s, where it continues to increase but at a lower rate. At this point, a maximum specific impulse of 250 s is achieved for $\epsilon_c = 2.40$ at $\phi = 1.5$ and $\dot{m}_{tot} = 0.454$ kg/s. As with the equivalence ratio flow condition set (Figure 5), at a given flow rate, the performance linearly increases with increasing constriction at the throat. Finally, the performance trends observed for both equivalence ratios are consistent with one another across the investigated flow rate range.

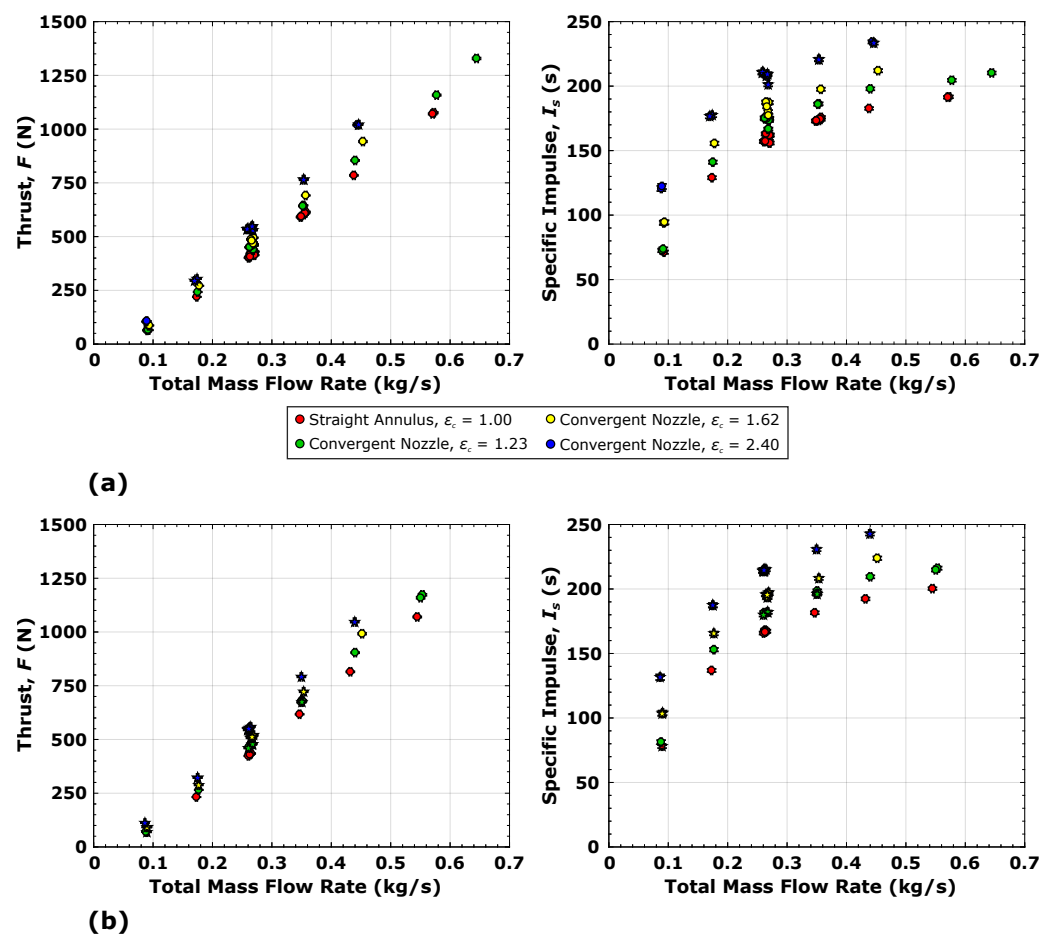


Figure 6. Performance summary for the $l_c = 76.2$ mm convergent nozzle study showing thrust F and specific impulse I_s for the total mass flow conditions at ϕ equaling (a) 1.15 and (b) 1.5, respectively. Depending on the flow condition and convergent nozzle geometry, the engine operates in either a corotating (\bullet) or counter-propagating mode (\star).

The fuel and oxidizer pressure drop (Figure 7) for the injector pair is calculated using the difference between the respective plenum pressures and equivalent average chamber pressure using CTAP1 (located closest to the detonation region). In general, the fuel pressure drop ranges from 780 to 2850 kPa for the equivalence ratio conditions at $\dot{m}_{\text{tot}} = 0.272$ kg/s (Figure 5) and 1470 to 4230 kPa for the propellant flow rate conditions at $\phi = 1.15$ (Figure 6). Similarly, the oxidizer pressure drop ranges from 1125 to 2160 kPa and 780 to 3540 kPa for the two flow condition sets, respectively. As the chamber pressure increases with increasing constriction at the throat, this causes the pressure drop to be decreased. Therefore, the pressure drops for $\epsilon_c = 1.23$, 1.62 and 2.40 nozzles on average are 4%, 13%, and 29% less than those for the straight annulus at similar flow conditions, but still remain choked.

Equivalent average chamber pressure measurements are taken at two axial locations within the annulus. CTAP1 is located at 8.89 mm from the injection plane, whereas CTAP2 is further downstream at 29.21 mm (see Figure 8d). The average pressures measured at the CTAP1 location for the three sets of flow conditions are shown in Figure 8a–c. For each of the nozzle geometries, the CTAP measurements closely correlate with the trends observed for the thrust measurements. Therefore, maximum pressure is reached from $\phi = 1.15$ to 1.5, and linearly increases with total propellant mass flow. For maximum performance at 0.272 kg/s, CTAP1 approaches 988 kPa for the most constricted $\epsilon_c = 2.40$ nozzle geometry, and increases to 1815 kPa at 0.453 kg/s. Overall, there is a greater than $3\times$ static chamber pressure increase on average for the most constricted nozzle geometry compared to the straight annular geometry, as well as an approximate $2\times$ increase for the $\epsilon_c = 1.62$ nozzle.

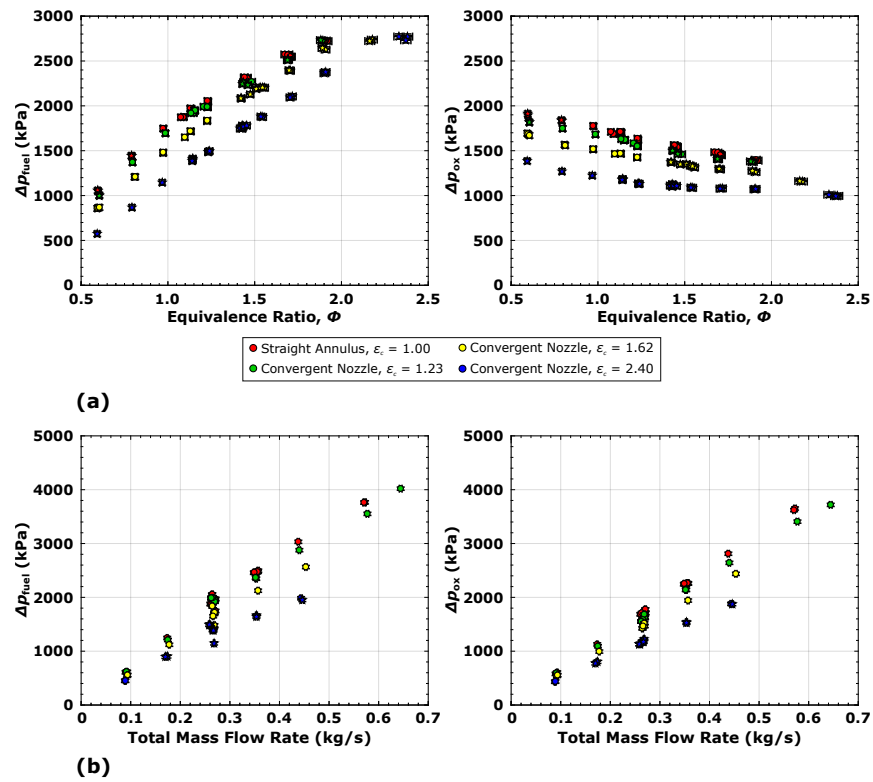


Figure 7. Injector pressure drop of the fuel (left) and oxidizer (right) for the (a) equivalence ratio (at $\dot{m}_{tot} = 0.272$ kg/s) and (b) mass flow rate conditions (at $\phi = 1.15$), respectively. Depending on the flow condition and convergent nozzle geometry, the engine operates in either a corotating (●) or counter-propagating mode (*).

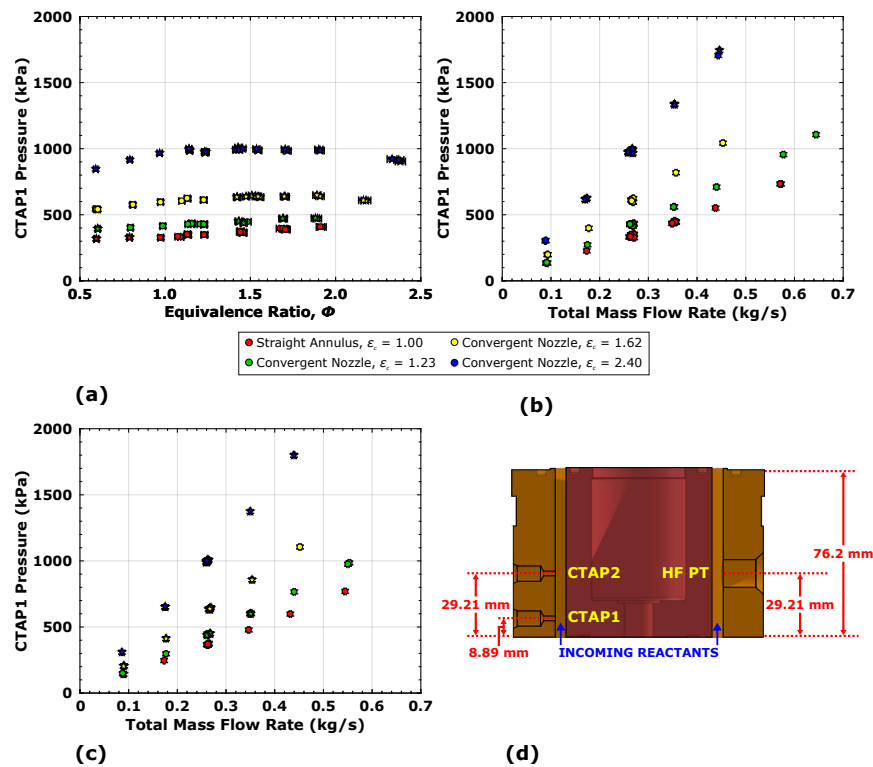


Figure 8. Equivalent average pressure measured at CTAP1 for the (a) equivalence ratio conditions and mass flow rate conditions at (b) $\phi = 1.15$ and (c) $\phi = 1.5$, as well as the (d) location of the measurement sites. Depending on the flow condition and convergent nozzle geometry, the engine operates in either a corotating (●) or counter-propagating mode (*).

To further analyze the effect of the various nozzle geometries on overall engine performance, it is instructive to compare the measured RDRE thrust to the theoretical thrust of an equivalent constant-pressure rocket engine with the same throat area and flow rate. The iterative approach for these comparisons is outlined in the work of Stechmann [12], and uses NASA's Chemical Equilibrium with Applications (CEA) code [20]. In summary, this approach uses the measured flow rates, CTAP1 pressure and nozzle dimensions for a single set of input conditions to calculate the characteristic velocity c^* of the ideal constant-pressure device. With this complete, the theoretical chamber pressure is then calculated using $p_{c,th} = c^* \dot{m}_{tot} / A_t$. Then c^* is updated as necessary using the revised theoretical chamber pressure. Once this iterative loop converges, the measured RDRE thrust is compared to the ideal thrust F_{th} calculated from the theoretical chamber pressure using $F_{th} = C_F p_{c,th} A_t$, where C_F is the thrust coefficient and A_t is the cross-sectional throat area. Results from this analysis for all flow conditions (see Figure 9) show that the generated thrust typically ranges from $F/F_{th} = 80\text{--}95\%$, which for the higher performing cases is comparable to state of the art conventional thrusters that typically operate around $F/F_{th} = 90\text{--}95\%$ [21]. Most notably, although the measured thrust is 27% higher on average for the most constricted nozzle, there is no appreciable increase when compared to the ideal thrust. In fact, for a given flow condition, there is no change among any of the nozzle geometries. This is likely due to the benefit of increased chamber pressure with increasing throat constriction, which is also accompanied with a complication/break-down of the local detonation structure due to longitudinal wave reflections emanating from the throat. Further analysis providing some physical insight into contributing factors that can lead to this break-down is given in the injector recovery analysis section of this manuscript (Section 5).

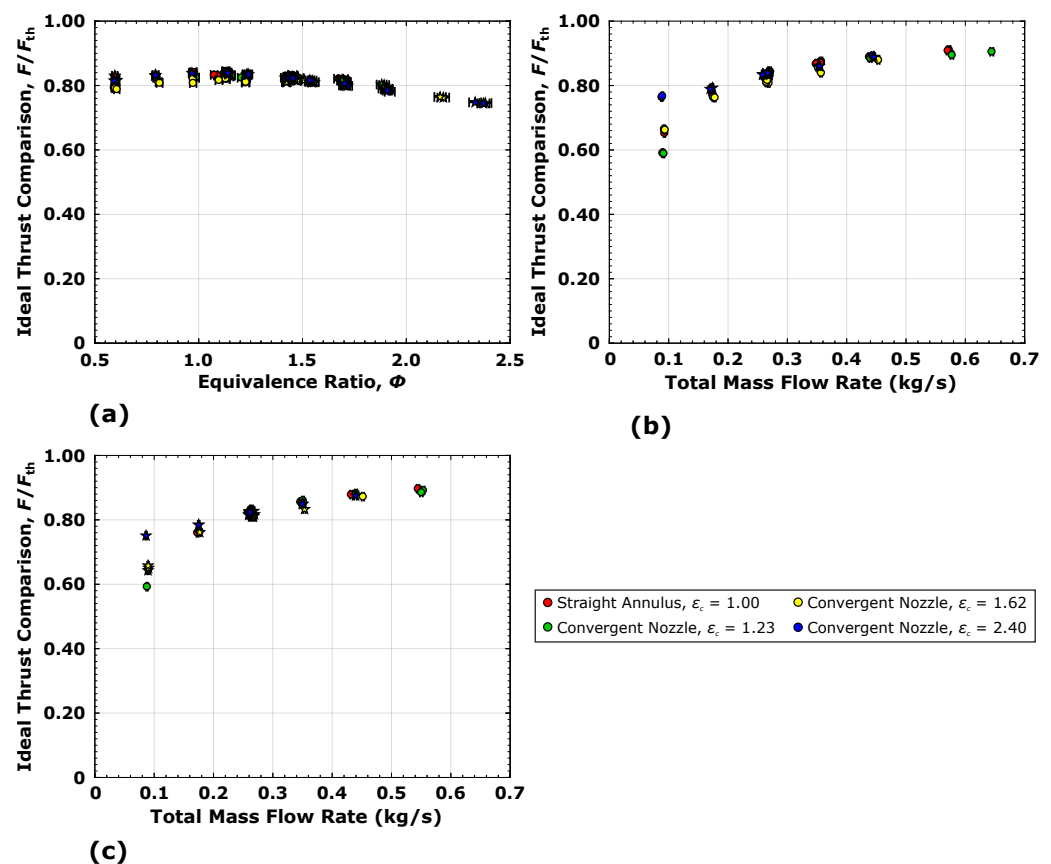


Figure 9. Ideal thrust comparison for the (a) equivalence ratio flow conditions at $\dot{m}_{tot} = 0.272$ kg/s, as well as the mass flow rate conditions for (b) $\phi = 1.15$ and (c) $\phi = 1.5$. Depending on the flow condition and convergent nozzle geometry, the engine operates in either a corotating (•) or counter-propagating mode (*).

3.2. Detonation Mode Characteristics

The average number of waves m and wave speed U_{wv} are determined using the image processing method reported previously [22]. This process entails automated analysis of the high-speed video images to track the integrated pixel intensity within 360 single-degree azimuthal bins around the annulus. This creates a detonation surface, which illustrates the propagation of all traveling detonations. A two-dimensional fast Fourier transform of the detonation surface data is then used to automatically extract both the number of waves m and associated operational frequency f_{det} . Combining these two parameters, the accompanying wave speed is determined using $U_{wv} = \frac{\pi d f_{det}}{|m|}$, where d is the mid-channel diameter of the annulus. This process has been shown to adequately extract modal properties throughout periods of steady-state propagation [5,13], as well as during transition events and counter-propagating phenomena [14,22]. Example data for a case exhibiting counter-propagating behavior with the $\epsilon_c = 2.40$ nozzle (see Figure 10) show that there is complex wave motion in both the clockwise (CW) and counterclockwise (CCW) directions as evidenced by the image sequence (Figure 10a) and detonation surface (Figure 10b). Nevertheless, the image processing technique is robust enough to separate both sets of opposing waves, which shows 8 CW waves as the dominant set traveling at 1280 m/s and 9 CCW opposing waves moving at 1200 m/s. As with the hot-fire measurements, the mode properties are averaged during the last 100 ms (bounded by the vertical dashed lines) for the reported results.

Average modal properties for the tests that vary equivalence ratio at constant flow rate show that the average number of waves ranges from 4 to 10 and corresponds to waves speeds from $U_{wv} \approx 1000$ –1700 m/s. For a given flow condition, the total number of waves is shown to consistently increase by $m = 1$ –2 with each increasing throat constriction across the entire equivalence ratio range (see Figure 11b). This increase in the number of waves is associated with a decrease in wave speed (see Figure 11c), as has been observed throughout the literature [1,2,5,6,12,23]. In addition, the increase in throat constriction from $\epsilon_c = 1.23$ to 2.40 corresponds with a substantial increase in counter-propagating behavior (denoted by a (\star) symbol), as all of the $\epsilon_c = 2.40$ tests exhibit this phenomenon. Comparing wave speeds from these tests to the theoretical ideal Chapman-Jouguet detonation velocities U_{CJ} calculated using CEA [24], the relative wave speeds range from 50 to 70% (Figure 11a). Generally, the highest achieved wave speeds are for the straight annulus cases, whereas the most constricted nozzle has the lowest wave speeds at approximately 50% of ideal and are generally insensitive to the flow condition, i.e., U_{wv} remains constant with changing ϕ . Furthermore, when comparing the average sound speed of combustion products c for CH_4/O_2 to the theoretical Chapman-Jouguet detonation velocity for these flow conditions, c/U_{CJ} is between 50 and 54%. Therefore, these cases with observed counter-propagating behavior are weaker operating modes and may be influenced by thermoacoustics. Specifically, it is possible that the counter-propagating behavior exhibited for the $\epsilon_c = 2.40$ nozzle causes detonation decoupling amongst the leading shocks and reaction zones of the traveling waves due to a combination of the fluctuation of the incoming propellant flows imposed by passing waves and longitudinal reflected shock waves local to the injection plane; this breakdown process could then cause the mode to be more thermoacoustic in nature than purely detonative, although non-ideal detonation propagation (i.e., lower strength detonation under the Chapman-Jouguet limit) for non-premixed injection has recently been shown in a complementary high-fidelity modeling effort by Lietz et al. [25]. Finally, the wave speed sensitivity to specific impulse (Figure 11d) for the various nozzle geometries demonstrates two separate trends. The first trend involves the straight annulus and $\epsilon_c = 1.23$ and 1.62 nozzles, which shows a relationship similar as the equivalence ratio sensitivity; the wave speeds on the higher and lower ends are approximately the same, with the highest specific impulse at the center of that range. The most constricted nozzle, however, exhibits a linear trend wherein the highest wave speeds (albeit lower than the other geometric cases) exhibit the highest specific impulse.

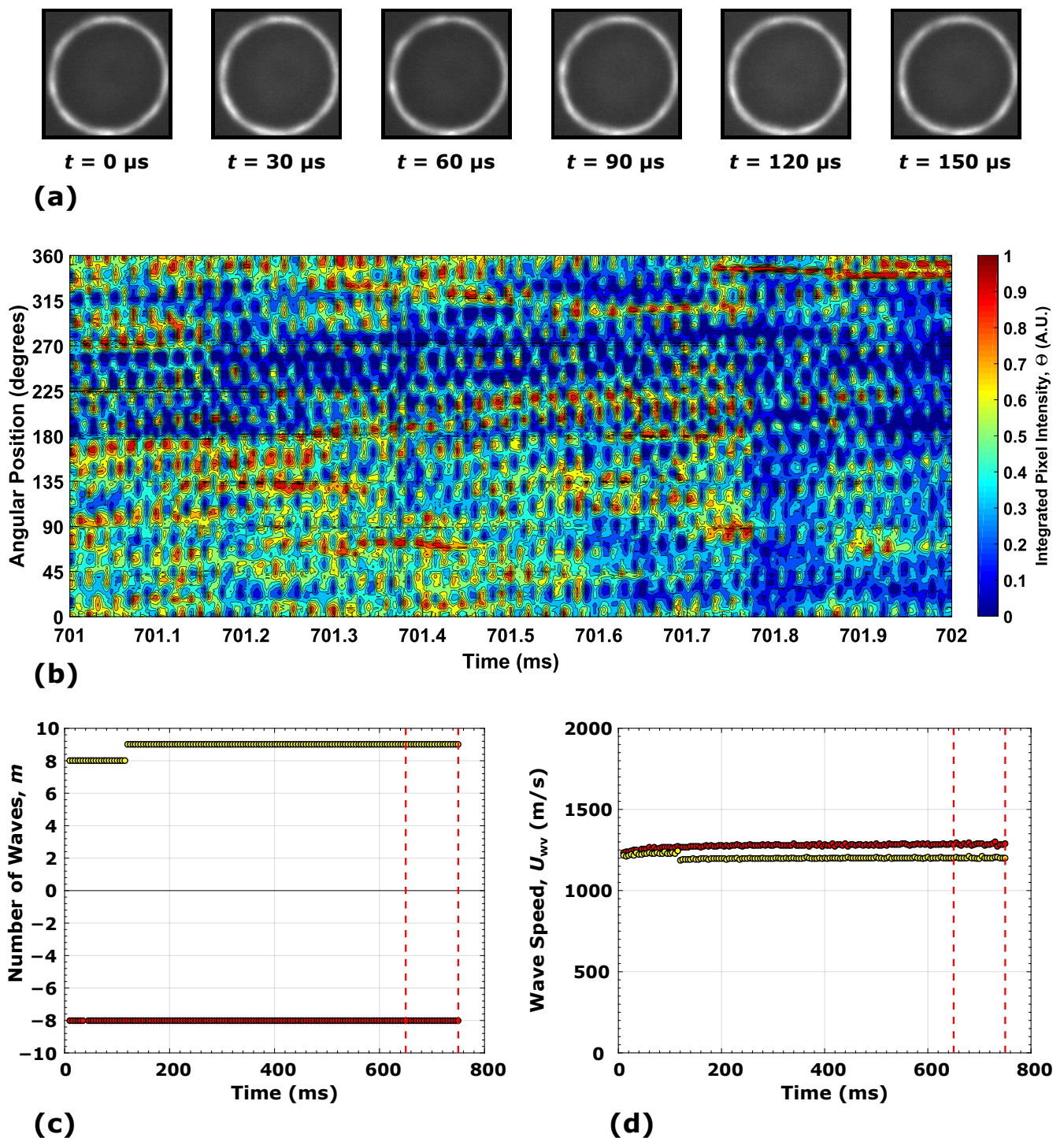


Figure 10. High-speed imaging summary for a counter-propagating mode exhibited with the $\epsilon_c = 2.40$ nozzle, depicting the (a) captured image sequence, (b) corresponding detonation surface, as well as the temporal histories of the (c) number of waves m and (d) average wave speed U_{wv} .

Example temporal histories taken from three tests in Figure 11 measured using the high-frequency pressure transducer flush mounted in the annulus show distinct responses depending on the type of detonation behavior present. A corotating mode only has waves traveling in a single direction, and generally exhibits well-defined steep-fronted pressure traces at high amplitude. Steep-fronted non-linear waves are shown for a 4 wave corotating case captured using the straight annulus (see Figure 12a), which cause the presence of higher harmonics within the frequency spectra. For this case, the operational

frequency (f_{det}) of the mode is measured to be 26.4 kHz from the high-speed images, which expectedly correlates with the maximum peak located at 26.4 kHz in the pressure transducer frequency spectra. A counter-propagating case with the straight annulus again shows steep-fronted behavior (see Figure 12b), but at a lower amplitude than the corotating mode case. Aside from this, the full width at half-maximum (FWHM) of the fundamental mode (see Figure 12b) spans a larger array of frequencies than the corotating case; this is indicative of the detonation process being less defined than the corotating mode. Nevertheless, the operational frequency captured in the high-speed images and the fundamental mode taken from the high-frequency pressure sensor both measure 31.7 kHz. Finally, the temporal history for a counter-propagating mode exhibited in the most constricted $\epsilon_c = 2.40$ nozzle has a steep-fronted, but more complicated response, as shown in Figure 12c. The accompanying frequency spectra show multiple integer peaks that are related to the operational frequency at 45.9 kHz. It is also noted that there are bifurcated peaks at the fundamental and first harmonic frequencies, which indicate the secondary set of waves that exists due to the counter-propagating mode behavior.

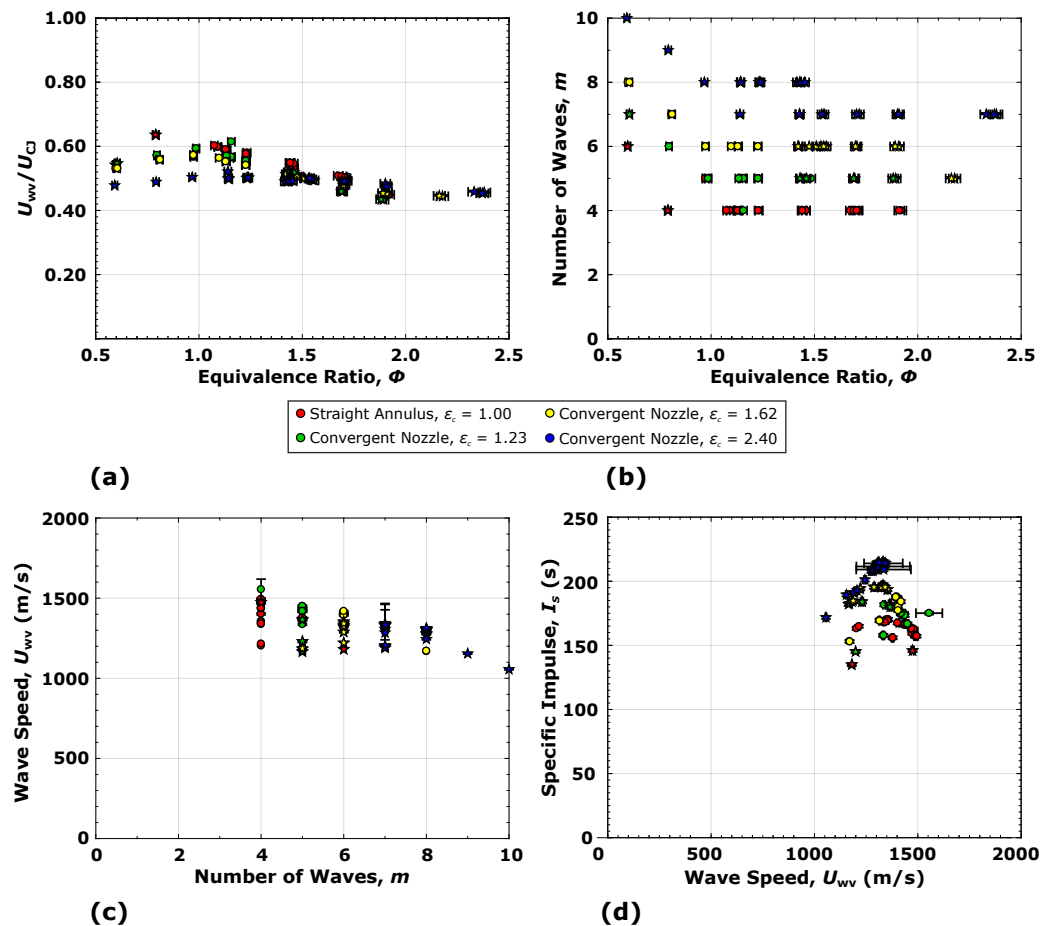


Figure 11. Summary of the detonation mode characteristics for the equivalence ratio conditions at $\dot{m}_{\text{tot}} = 0.272$ kg/s, depicting the (a) wave speed percentage of ideal and (b) number of waves m , as well as the wave speed sensitivity to the (c) number of waves and (d) specific impulse I_s . Depending on the flow condition and convergent nozzle geometry, the engine operates in either a corotating (●) or counter-propagating mode (★).

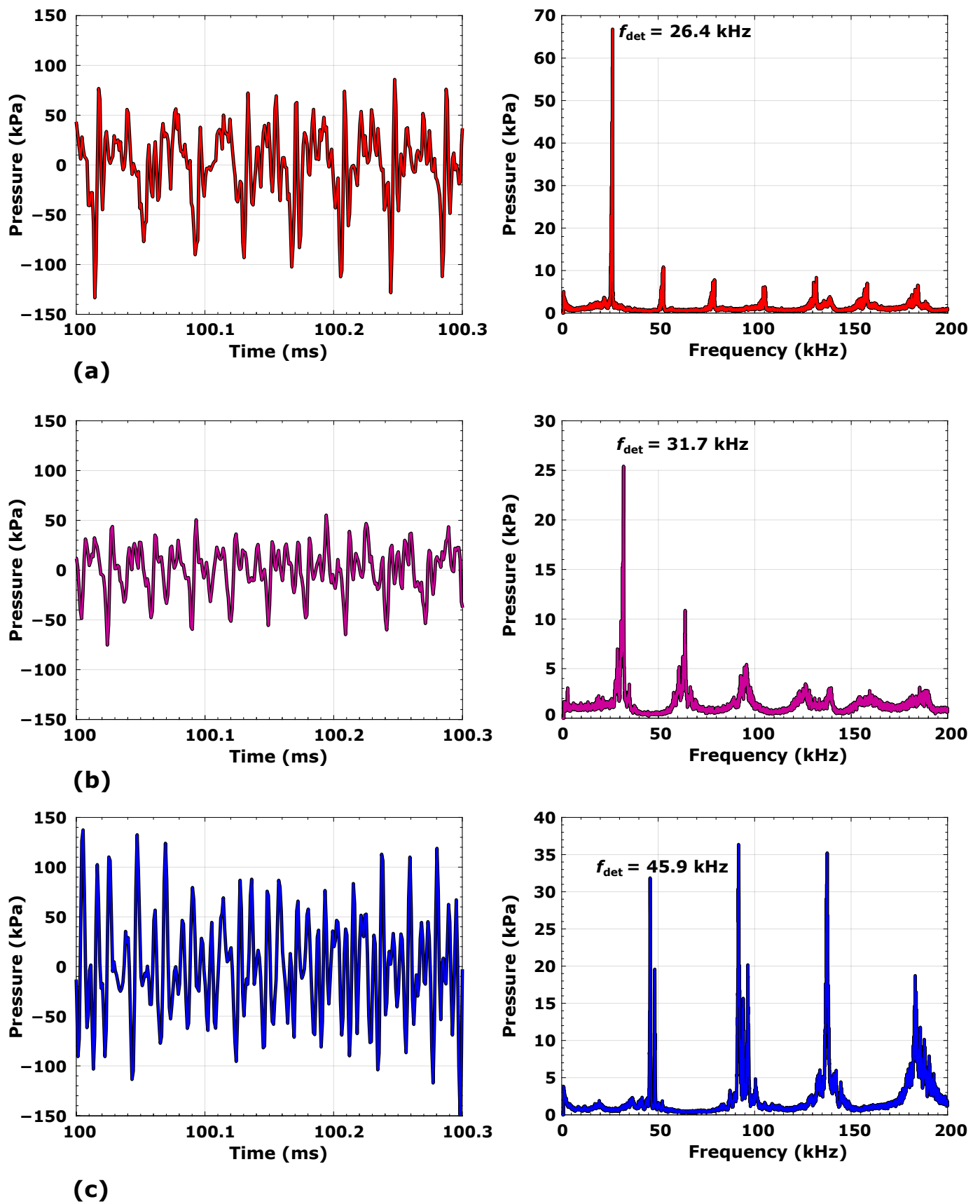


Figure 12. Example temporal pressure histories (left) and corresponding frequency spectra (right) of the following modal behavior: (a) corotating mode for $\epsilon_c = 1.00$ at $m = 4$ waves with $f_{\text{det}} = 26.4$ kHz, (b) counter-propagating mode for $\epsilon_c = 1.00$ at $m = 6$ waves with $f_{\text{det}} = 31.7$ kHz, and (c) counter-propagating mode for $\epsilon_c = 2.40$ at $m = 8$ waves with $f_{\text{det}} = 45.9$ kHz.

A summary of the modal properties for the range of mass flow rate conditions at $\phi = 1.15$ generally show trends (see Figure 13) similar to the previous conditions of Figure 11. As with the equivalence ratio tests, the number of waves increases by $m = 1$ – 2 waves for a given flow condition with increasing throat constriction (see Figure 13b), and this increase in the number of waves is again accompanied by a decrease in wave speed (Figure 13c). In addition, increasing the total mass flow rate causes an increase in the total number of waves, consistent to the work of Bykovskii and Zhdan [26]. However, the modal wave speeds captured throughout the \dot{m}_{tot} range are fairly constant for a given annular geometry, with the straight annulus having the highest $U_{\text{wv}}/U_{\text{CJ}}$ between 65 and 70% (see Figure 13a) and the most constricted $\epsilon_c = 2.40$ nozzle at a value of approximately 50%. Therefore, it appears that the overall modal wave speed is much more sensitive to equivalence ratio than incoming propellant mass flux, providing another indication that efficient mixing through injection (e.g., local equivalence ratio) is a key parameter to increasing local detonation performance, i.e., wave speed and detonation front coupling [13]. Finally, the insensitivity of the wave speed to global performance for these annular geometries with increasing \dot{m}_{tot} is evident in Figure 13d, as each annular design shows a vertical line with near constant U_{wv} for increasing specific impulse.

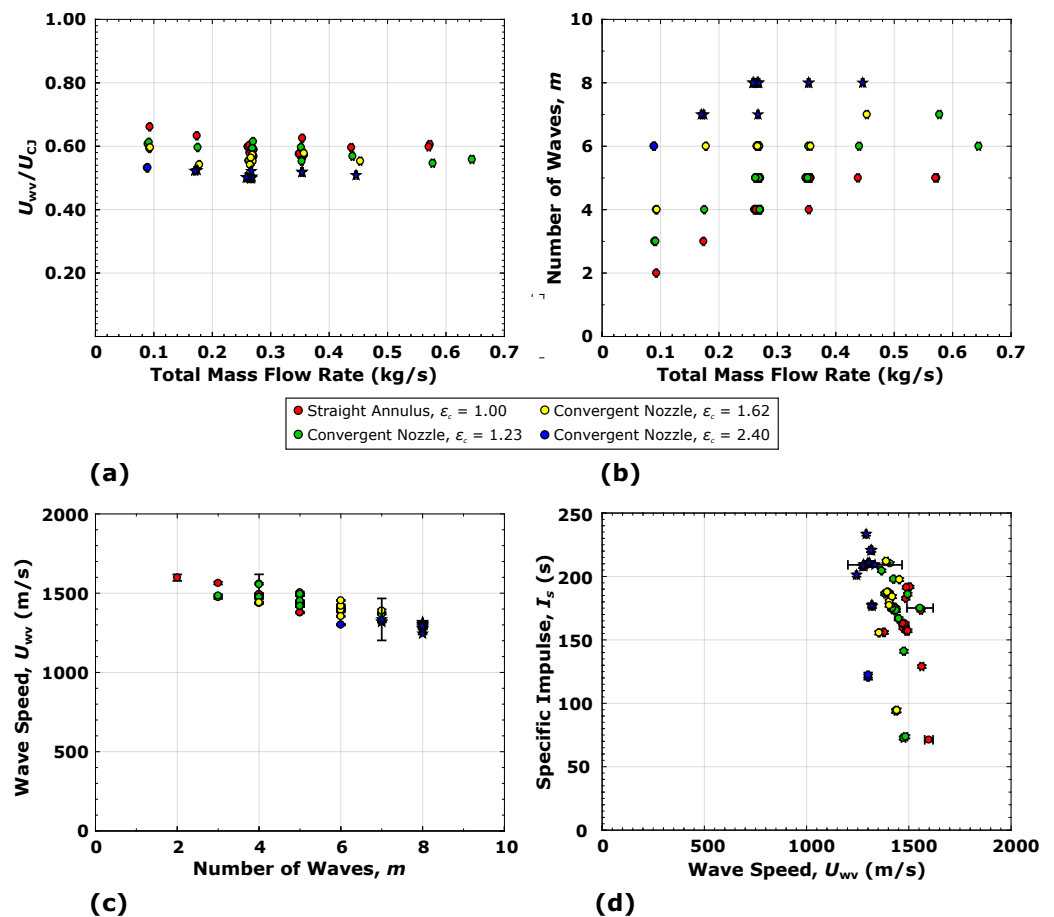


Figure 13. Summary of the detonation mode characteristics for the total mass flow conditions at $\phi = 1.15$, depicting the (a) wave speed percentage of ideal and (b) number of waves m , as well as the wave speed sensitivity to the (c) number of waves and (d) specific impulse I_s . Depending on the flow condition and convergent nozzle geometry, the engine operates in either a corotating (\bullet) or counter-propagating mode (\star).

4. Convergent Nozzle Study: Reduced Length Geometries

4.1. Engine Operability and Performance

To investigate the effect of chamber length on the performance, operability and detonation characteristics of the engine, the same flow condition matrix as shown in Figure 3 was completed for the straight annulus and $\epsilon_c = 2.40$ nozzle configurations with the annular length reduced by half of the original, i.e., $l_c = 38.1$ mm; these results are then compared against their complementary full-length geometries to distinguish any apparent differences. For the shortened geometries, detonation is successfully achieved across the entire flow condition matrix for both the equivalence ratio range from $\phi = 0.5$ – 2.5 and $\dot{m}_{\text{tot}} = 0.091$ – 0.680 kg/s, indicating that there is no appreciable drop-off in engine operability for the shorter chamber length. Global engine performance for the range of equivalence ratio conditions shows that there is no significant reduction for both reduced length geometries across the whole range (see Figure 14). In fact, a few conditions at peak performance near $\phi = 1.15$ have a 6% increase for the reduced length $\epsilon_c = 2.40$ configuration over the $l_c = 76.2$ mm equivalent. This is one indication that the shortened annular length geometry may be closer to the optimal combustor length for effective RDRE operation using gaseous propellants.

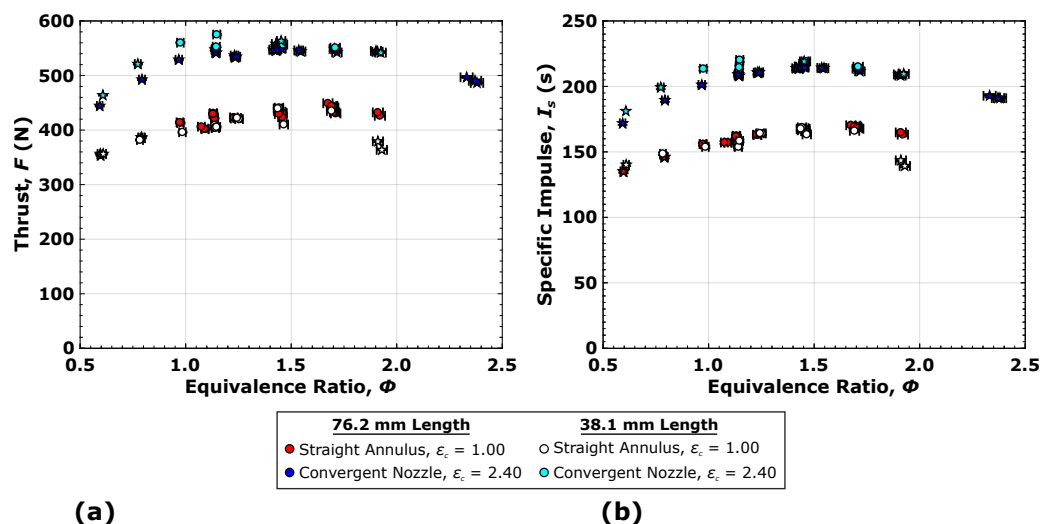


Figure 14. Performance summary for the shortened annular length study showing (a) thrust F and (b) specific impulse I_s for the equivalence ratio flow conditions at $\dot{m}_{\text{tot}} = 0.272$ kg/s. Depending on the flow condition and convergent nozzle geometry, the engine operates in either a corotating (●) or counter-propagating mode (★).

The thrust and specific impulse for the two total mass flow rate condition sets demonstrate similar trends, where there are no significant decreases noted for either the $l_c = 38.1$ mm straight annulus or $\epsilon_c = 2.40$ nozzle design (see Figure 15). As seen previously for the full annular length results, the two $l_c = 38.1$ mm geometries both show a linear increase in thrust from $\dot{m}_{\text{tot}} = 0.091$ – 0.680 kg/s with the same respective slopes as their $l_c = 76.2$ mm equivalent. Furthermore, specific impulse similarly increases with total mass flow rate for the shortened straight annulus and $\epsilon_c = 2.40$ nozzle, where I_s begins to increase at a slower rate beginning at \dot{m}_{tot} equaling 0.340 kg/s. Finally, for a majority of the $l_c = 38.1$ mm, $\epsilon_c = 2.40$ nozzle tests, there appears to be a small but notable increase in specific impulse over the $l_c = 76.2$ mm, $\epsilon_c = 2.40$ nozzle tests.

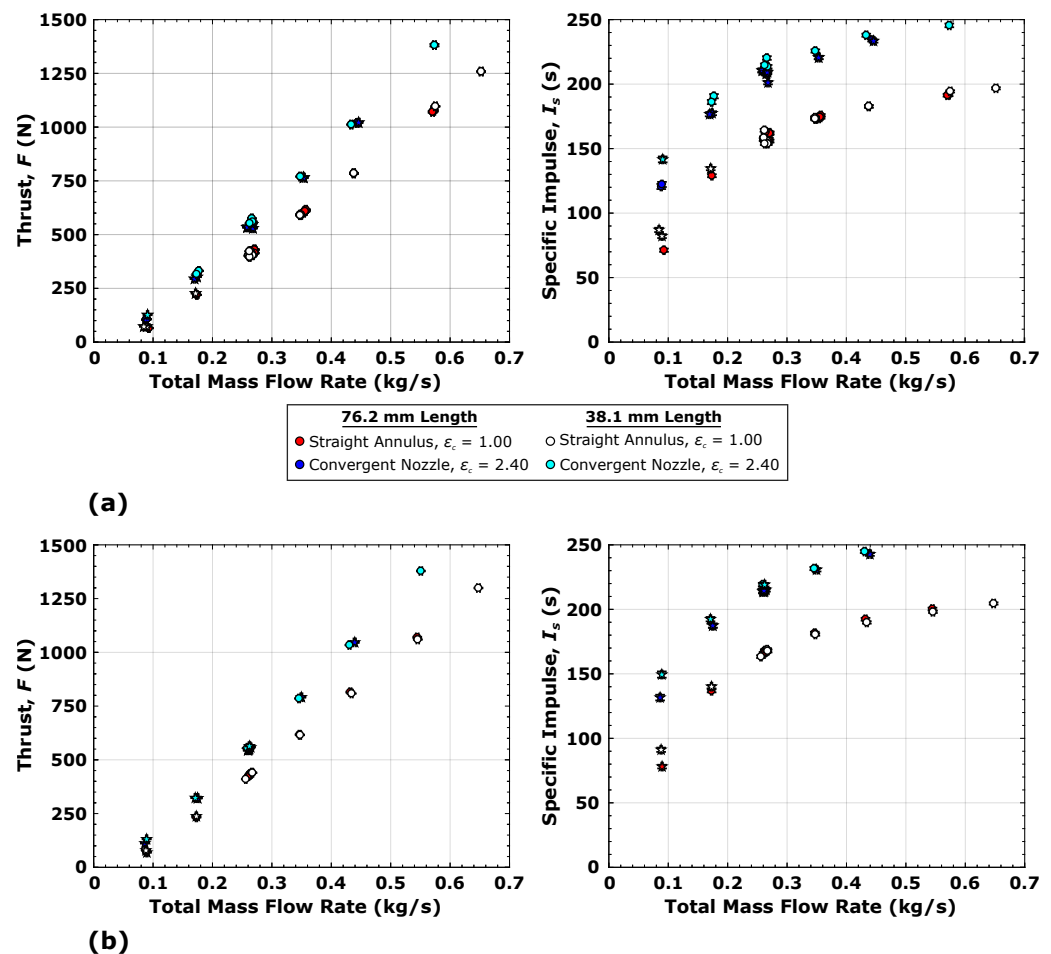


Figure 15. Performance summary for the shortened annular length study showing thrust F and specific impulse I_s for the total mass flow conditions at ϕ equaling (a) 1.15 and (b) 1.5, respectively. Depending on the flow condition and convergent nozzle geometry, the engine operates in either a corotating (\bullet) or counter-propagating mode (\star).

For the shortened geometries, only one CTAP sensor is present within the chamber, at the same axial location as the closest sensor to the detonation zone for the $l_c = 76.2$ mm configurations, i.e., 8.89 mm. In general, CTAP1 measurements for both straight annulus length designs consistently have the same pressure levels for all investigated flow conditions, which again correlate well with global performance (see Figure 16). However, the CTAP1 pressure for the $l_c = 38.1$ mm, $\epsilon_c = 2.40$ nozzle is notably higher than the $l_c = 76.2$ mm design for all flow conditions. On average, this increase is approximately 13%, which provides one indication that the high pressure zone associated with detonation is pushed slightly downstream from the injection plane for the $l_c = 38.1$ mm configuration.

To assess the reduction in chamber length on performance efficiency, a comparison similar to the aforementioned theoretical thrust comparison is carried out for both of the $l_c = 38.1$ mm configurations. As shown in Figure 17, there is no significant decrease in F/F_{th} for the shortened straight annulus across the investigated flow conditions compared to the $l_c = 76.2$ mm straight annulus. The shortened ϵ_c nozzle actually provides maximum theoretical efficiency for all geometries at the equivalence ratios around peak performance ($\phi = 1.0$ – 1.15), which is $F/F_{th} \approx 90\%$. Therefore, this indicates that there are some potential advantages of reducing these annular configurations axially for RDEs to make them more compact. Specifically, this result indicates that reduction in annular length may lead to higher performance RDREs. Further studies to identify the limits to this trend are warranted.

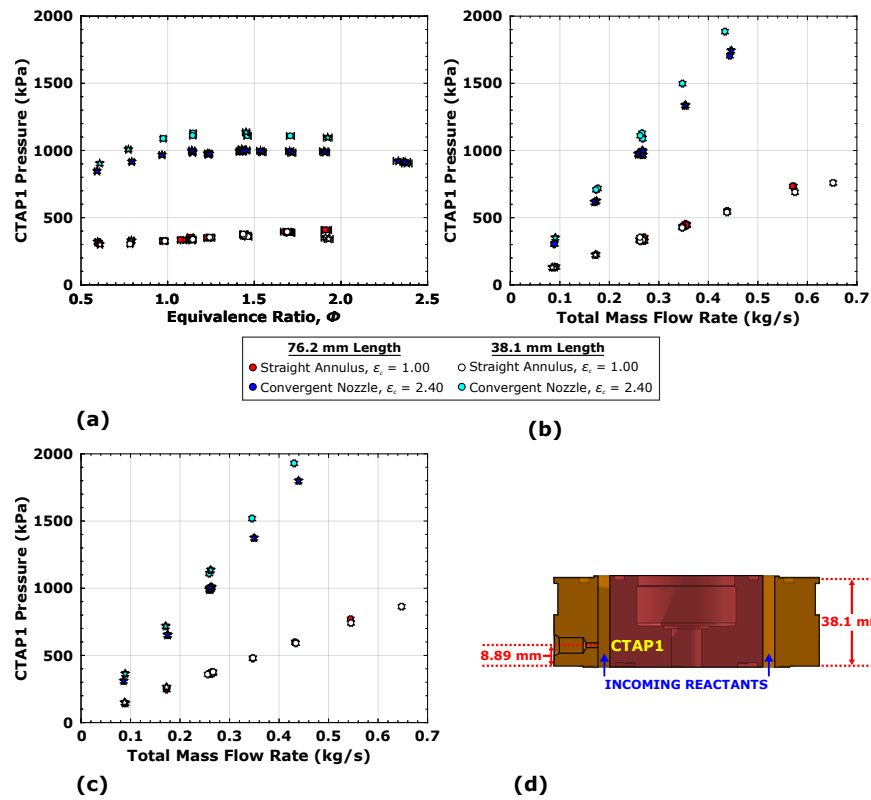


Figure 16. Equivalent average pressure measured at CTAP1 for the (a) equivalence ratio conditions and mass flow rate conditions at (b) $\phi = 1.15$ and (c) $\phi = 1.5$, as well as the (d) location of the measurement sites for the reduced length geometry. Depending on the flow condition and convergent nozzle geometry, the engine operates in either a corotating (\bullet) or counter-propagating mode (\star).

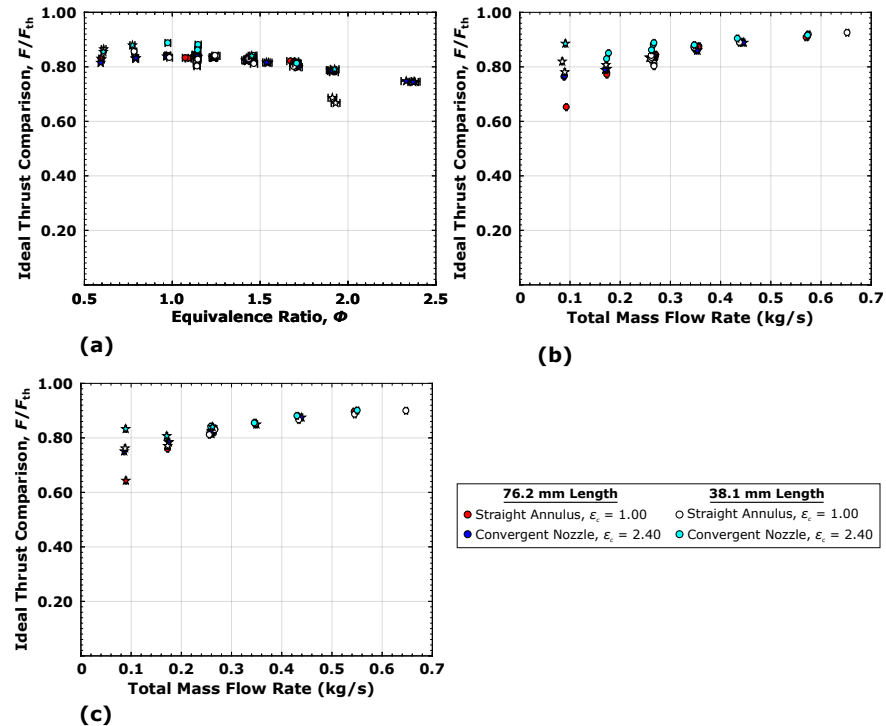


Figure 17. Ideal thrust comparison for the (a) equivalence ratio flow conditions at $m_{tot} = 0.272$ kg/s, as well as the mass flow rate conditions for (b) $\phi = 1.15$ and (c) $\phi = 1.5$. Depending on the flow condition and convergent nozzle geometry, the engine operates in either a corotating (\bullet) or counter-propagating mode (\star).

4.2. Detonation Mode Characteristics

Average modal properties of the $l_c = 38.1$ mm designs for the equivalence ratio conditions show that the shortened axial chamber length plays a large role (see Figure 18). Specifically, the number of waves observed using the shortened straight annulus is generally reduced by $m = 1$ wave compared to the longer straight annulus for $\phi = 0.2$ – 2.0 . This reduction is accompanied by an increase in wave speed, where a maximum wave speed is observed for the shortened straight annulus at $\phi = 1$, which corresponds to $U_{wv}/U_{CJ} = 70\%$ and $m = 3$ waves. Similarly to the straight annular geometries, counter-propagating behavior is only observed for significantly off-stoichiometric conditions, i.e., primarily lean conditions, but also occasionally very fuel rich. Unlike the full-length annulus with the $\epsilon_c = 2.40$ nozzle, counter-propagating behavior is not regularly observed for the shortened annulus with a similar nozzle. This may be attributed to the change in detonation-injection coupling due to the physical throat location being shifted much closer to the injection plane for the $l_c = 38.1$ mm design. If this longitudinal coupling is thermoacoustic in nature as suggested by Paxson and Schwer [9], altering the axial wave reflection plane can spatially shift the location of maximum heat release, which will either drive or damp the instability depending on its phasing with oscillatory pressure and spatial location. This in turn will alter the amount of propellant feed modulation present, affecting the mixing uniformity of the reactant fill zone, which directly influences the number of waves observed and the prevalence of counter-propagating behavior [25]. It should be noted that although the shortened $\epsilon_c = 2.40$ nozzle geometry does not exhibit primarily counter-propagation of the waves, the number of waves is generally the highest for a given flow condition, mostly between $m = 9$ – 10 waves. This causes the wave speeds to be close to that of the $l_c = 76.2$ mm, $\epsilon_c = 2.40$ nozzle, approximating $U_{wv}/U_{CJ} = 50\%$. This again suggests the possibility that these propagating modes are influenced by longitudinal thermoacoustic fluctuations, as the sound speed of the combustion products of CH_4/O_2 falls within this range. Finally, there appears to be only a weak correlation between performance and wave speed for the shortened $\epsilon_c = 2.40$ nozzle, with performance increasing somewhat linearly with wave speed (see Figure 18d).

As with the equivalence ratio conditions of Figure 17, the two mass flow rate test sets exhibit similar modal property trends. As shown in Figure 19, the shortened straight annulus typically excites modes with wave speeds that are on the same order as the full-length configuration for a given flow condition. The shorter $l_c = 38.1$ mm, $\epsilon_c = 2.40$ nozzle geometry again does not have active counter-propagating behavior aside from the extremely low flow rate case at \dot{m}_{tot} less than 0.136 kg/s. As with the equivalence ratio test set, the shortened $\epsilon_c = 2.40$ nozzle typically has the highest number of waves, again typically $m = 9$ waves; this corresponds to observed wave speeds that approximate $U_{wv}/U_{CJ} = 50\%$. Nevertheless, the combination of slightly higher performance for the shortened geometries along with the reduction in counter-propagating behavior suggests that these promising compact axial designs need to be further studied and optimized.

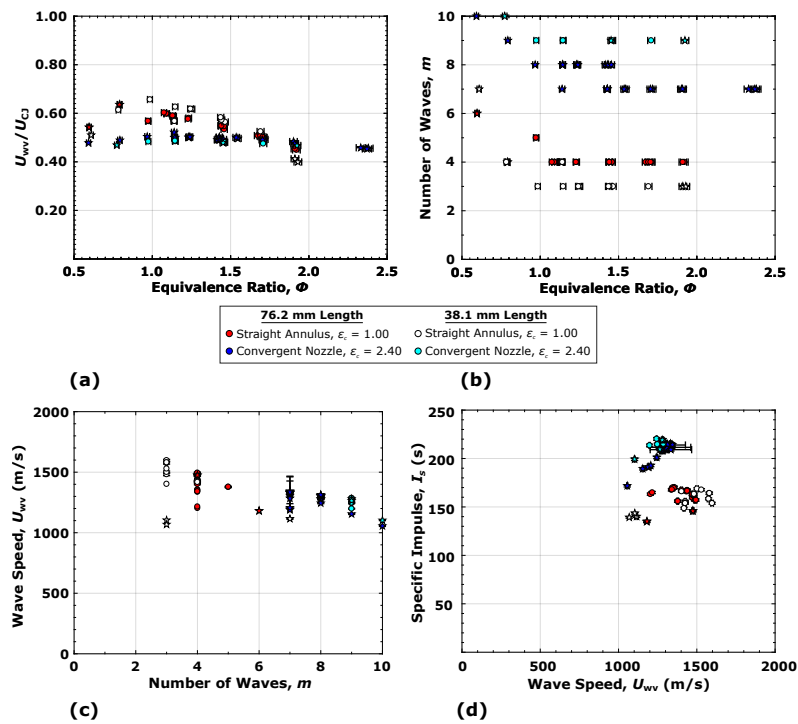


Figure 18. Summary of the detonation mode characteristics for the equivalence ratio conditions at $\dot{m}_{tot} = 0.272$ kg/s, depicting the (a) wave speed percentage of ideal and (b) number of waves m , as well as the wave speed sensitivity to the (c) number of waves and (d) specific impulse I_s . Depending on the flow condition and convergent nozzle geometry, the engine operates in either a corotating (●) or counter-propagating mode (★).

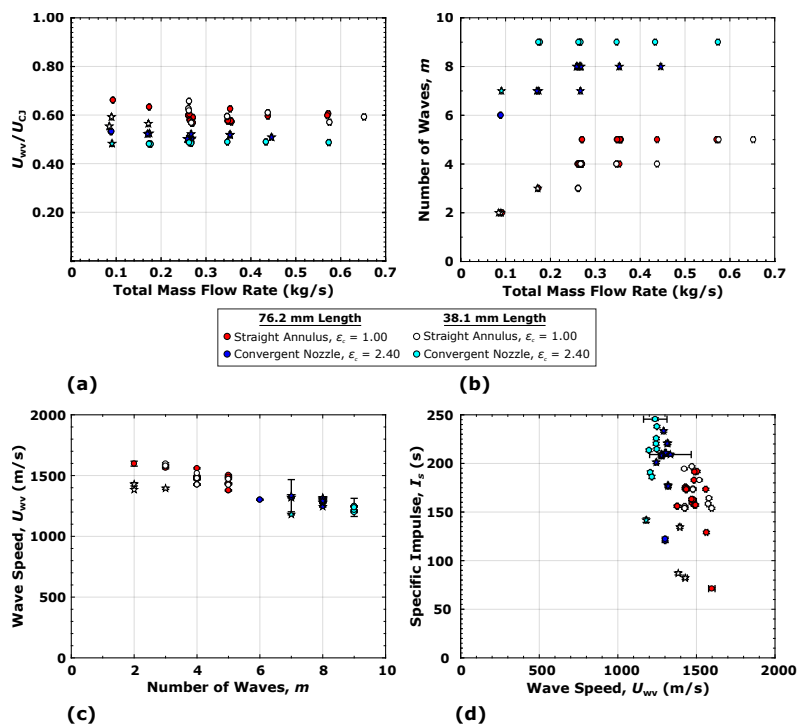


Figure 19. Summary of the detonation mode characteristics for the total mass flow conditions at $\phi = 1.15$, depicting the (a) wave speed percentage of ideal and (b) number of waves m , as well as the wave speed sensitivity to the (c) number of waves and (d) specific impulse I_s . Depending on the flow condition and convergent nozzle geometry, the engine operates in either a corotating (●) or counter-propagating mode (★).

5. Injector Recovery Analysis

To provide more insight into the physical phenomena which can cause the detonation structure to break down due to wave reflections in the vicinity of the injectors (e.g., transverse wave reflections emanating from injection orifices or longitudinal reflections from a physical throat), an idealized analysis is performed to illustrate how mass flow rate and equivalence ratio fluctuate due to chamber pressure oscillations local to the injection plane. This analysis uses the inlet flow conditions of a straight annulus geometry firing at $\phi = 1.07$ and $\dot{m}_{\text{tot}} = 0.263$ kg/s; this test corresponds to $m = 4$ waves moving at approximately 60% of theoretical, i.e., a high performing case for the equivalence ratio conditions. A summary of these inlet conditions is presented in Table 2, which shows injector plenum feed pressures approximating 2000–2200 kPa with an average chamber pressure of 334 kPa.

Table 2. Summary of flow parameters for a straight annulus run with $\phi = 1.07$ and $\dot{m}_{\text{tot}} = 0.263$ kg/s.

\dot{m}_{ox} (kg/s)	\dot{m}_{fuel} (kg/s)	\dot{m}_{tot} (kg/s)	ϕ	$p_{\text{fuel,pln}}$ (kPa)	$p_{\text{ox,pln}}$ (kPa)	CTAP1 (kPa)	m	c/U_{CJ}
0.207	0.056	0.263	1.07	2207	2044	334	4	0.60

As mentioned earlier, the injectors normally operate at choked conditions. Under the choked condition, the mass flow rate is only a function of upstream pressure and does not change due to alterations of the pressure downstream of the orifice (as long as the choked condition persists). As such, the mass flow rate for gaseous choked flow through an injector orifice can be written as [27,28]

$$\dot{m}_g = C_d A_{\text{inj}} \sqrt{\gamma p_{\text{pln}} \rho_{\text{pln}} \left(\frac{2}{\gamma + 1} \right)^{\frac{\gamma+1}{\gamma-1}}}, \quad (1)$$

where C_d is the orifice discharge coefficient, A_{inj} is the injector orifice cross-sectional area, γ is the specific heat ratio and p_{pln} and ρ_{pln} are the upstream plenum pressure and density, respectively.

From classical compressible flow [29], choked flow will persist as long as the orifice pressure ratio p_c/p_{pln} is operated under a value defined as the critical pressure ratio, p_{crit} , which is given by

$$p_{\text{crit}} = \left(\frac{2}{\gamma + 1} \right)^{\frac{\gamma}{\gamma-1}}. \quad (2)$$

For the fuel and oxidizer plenum conditions of the baseline test, the critical pressure ratios are $p_{\text{crit}} = 0.53$ and 0.52 , respectively. However, when a wave passes over a given injection site, the flow can momentarily become unchoked due to the locally high pressure associated with the detonation. Under unchoked conditions, the mass flow rate is now affected by downstream pressure oscillations and can even result in a momentary flow reversal condition if the downstream pressure becomes sufficiently large. The mass flow rate for unchoked gaseous propellant flow can be estimated using [28]

$$\dot{m}_g = C_d A_{\text{inj}} \sqrt{2 p_{\text{pln}} \rho_{\text{pln}} \left(\frac{\gamma}{\gamma-1} \right) \left[\left(\frac{p_c}{p_{\text{pln}}} \right)^{\frac{2}{\gamma}} - \left(\frac{p_c}{p_{\text{pln}}} \right)^{\frac{\gamma+1}{\gamma}} \right]}, \quad (3)$$

where a flow reversal event is denoted by $\left(\frac{p_c}{p_{\text{pln}}} \right)^{(\gamma+1)/\gamma} > \left(\frac{p_c}{p_{\text{pln}}} \right)^{2/\gamma}$.

To model the periodic pressure and temperature cycles associated with detonation wave passage, synthetic profiles of detonation waveforms ranging from low amplitude weak detonation to high amplitude detonation at the theoretical Chapman-Jouguet limit shown in Figure 20 are used. All of the simulated waveforms are steep-fronted in nature, even for the low amplitude cases as the objective of this analysis is primarily to isolate oscil-

latory pressure amplitude effects on the local flow rate. Therefore, four cases are considered where the pressure amplitude rise across the detonation varies from $p_{\text{rise}} = 5$ –30. Using NASA's CEA code, a CH_4/O_2 detonation for $\phi = 1.07$ and the respective plenum conditions, the theoretical Chapman-Jouguet pressure ratio is also $p_{\text{rise}} \approx 30$ and the accompanying temperature ratio is $T_{\text{rise}} \approx 13$; the ratio between the pressure and temperature rise ratios are held constant for all four of the investigated test cases. These test cases are summarized in Table 3.

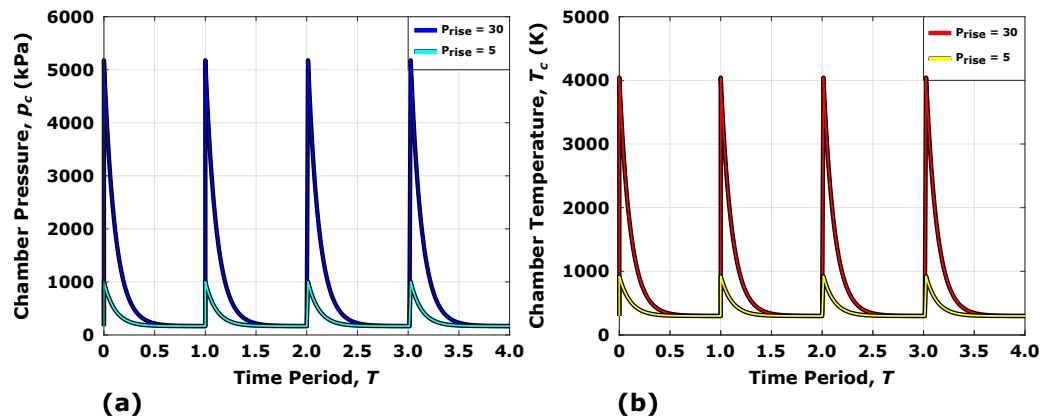


Figure 20. Synthetic data of oscillatory (a) pressure and (b) temperature for a CH_4/O_2 detonation ranging from low amplitude ($p_{\text{rise}} = 5$) to the theoretical Chapman-Jouguet detonation limit ($p_{\text{rise}} = 30$).

Using the synthetic data generated for the four sets of test conditions, mass flow rates for individual injector orifices of the fuel and oxidizer are calculated using a combination of Equations (1) and (3), depending on the flow choke condition. The orifice pressure ratio is found at every instance throughout the temporal cycle and is used as the determination whether the choked or unchoked condition applies. In the event of a backflow event occurring, the mass flow rate is found using the same equations but switching the respective upstream and downstream conditions as necessary.

The lowest amplitude detonation case $p_{\text{rise}} = 5$ does not have a high enough pressure rise to unchoke the flow. This can be seen in Figure 21a, where the mass flow rates of the fuel and oxidizer injectors are constant throughout the time period. This also corresponds to the expected, constant equivalence ratio of $\phi = 1.07$. While it may appear desirable to operate under choked conditions at all times, this counteracts one of the benefits of a detonation-based propulsion system in which the injection pressures can theoretically be significantly reduced from traditional designs [5]. Furthermore, choked flow is difficult to maintain completely during operation at high detonation amplitudes. Therefore, the flow response observed in the cases above $p_{\text{rise}} = 10$ better illustrates the effect of sharp pressure rises on fuel and oxidizer flow rates, and thus on the local equivalence ratio in an RDRE. In the $p_{\text{rise}} = 10$ case (see Figure 21b), periodic unchoking (wave passage) events (highlighted in yellow) occur during the peak rise events. This results in reduction of both the fuel and oxidizer flow rates from their nominal values. These flow rates eventually recover when periods of choked flow resume (highlighted in cyan) without any flow reversal present. It should be noted that the average pressure associated with the synthetic data for this case is $p_{c,\text{avg}} = 356$ kPa, which is close to the baseline experiment pressure of $p_{\text{CTAP}} = 334$ kPa. Therefore, this case is the most analogous to the experimental conditions reported above. Under this periodic choking and unchoking process, the local equivalence ratio for the considered injector pair oscillates up to 25% higher than the desired condition and ranges from $\phi = 1.07$ –1.34. This case illustrates that there are inherent local flow rate fluctuations present during engine operation, with accompanying variations in equivalence ratio.

Table 3. Summary of the investigated test cases.

p_{rise} Ratio	T_{rise} Ratio	$p_{c,\text{avg}}$ (kPa)	$T_{c,\text{avg}}$ (K)	\dot{m} Oscillation Event
5.00	2.10	262	369	None (Fully Choked)
10.0	4.19	356	439	Partially Unchoked
20.0	8.38	545	581	Small Magnitude Backflow
30.0	12.57	734	722	Large Magnitude Backflow

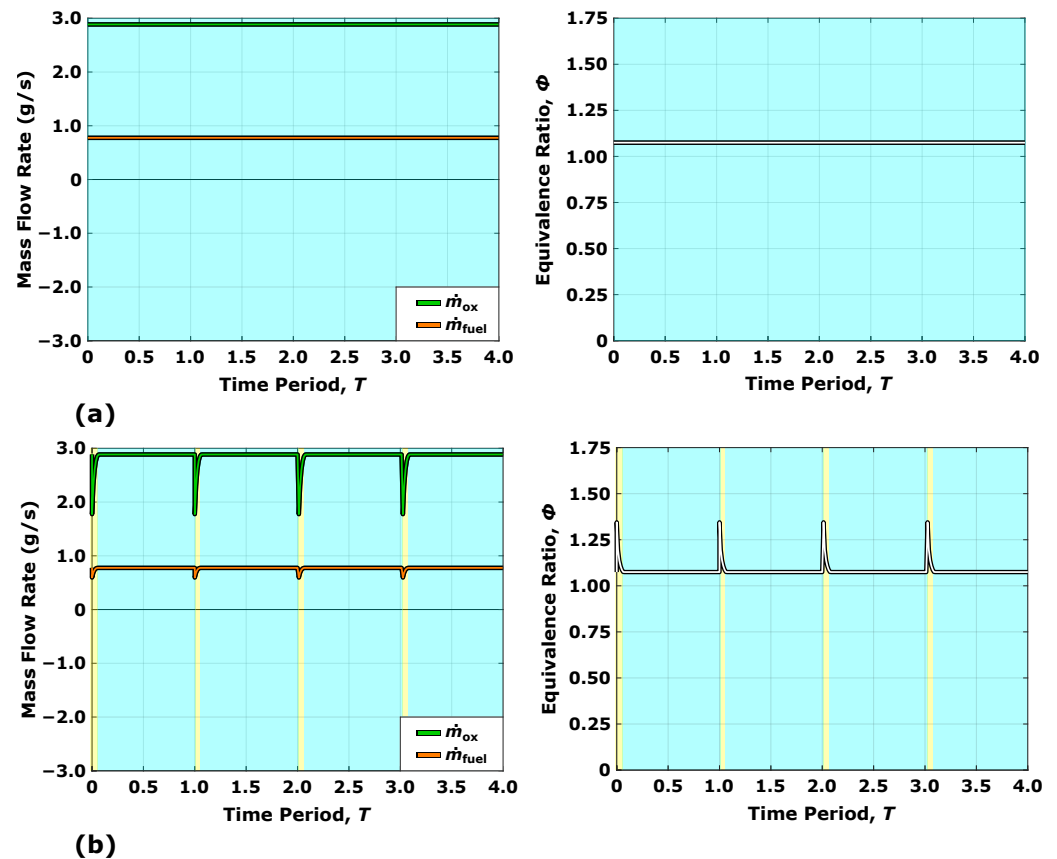


Figure 21. Temporal histories for the fuel and oxidizer mass flow rate (left) and corresponding equivalence ratio ϕ (right), for the (a) $p_{\text{rise}} = 5$ and (b) $p_{\text{rise}} = 10$ cases. Note that the cyan highlighted periods denote choked flow and yellow denotes unchoked flow.

The two highest pressure rise cases $p_{\text{rise}} = 20$ and 30 both produce flow reversal events to varying degrees (see Figure 22). The $p_{\text{rise}} = 20$ case has a backflow event which is smaller in duration than the highest case. The flow reversal events (shown in magenta and red for unchoked and choked flows, respectively) sees the flow rates of both the fuel and oxidizer sharply decay to a minimum, which then recover after the wave passes. Similar behavior is exhibited for the Chapman-Jouguet condition detonation (i.e., $p_{\text{rise}} = 30$ case), except for the flow rate oscillations being higher in amplitude and the recovery time being longer in duration. The corresponding equivalence ratio fluctuations span a large range from $\phi = 0$ (i.e., no reactants present due to flow reversal) to 1.35 for the $p_{\text{rise}} = 20$ case and up to $\phi = 1.50$ for the maximum. Again, this shows that local equivalence ratio fluctuations can become very significant during operation of high-amplitude detonation propagation.

As this idealized analysis demonstrates the potential for large amplitude ϕ oscillations present in the reactant fill region due to the passing detonations, there must be sufficient recovery time for the injector flows both to regain their expected flow rates and fully mix prior to the next wave passage event. This recovery event is crucial to effectively create a uniform reactant fill zone for the detonation to propagate through for high detonative performance, as injector geometries with intentionally poor mixing [13] have consistently

demonstrated a breakdown in well-defined detonation mode structure in favor of more complicated/less periodic, counter-propagating behavior. While the passing detonations cause the need for injection recovery, it is possible that the longer annulus constricted cases have traveling longitudinal wave reflections emanating from the area constriction back to the fill region that disrupt the incoming injector flow rates during this recovery time, further striating the reactant fill zone prior to the next wave arrival. This flow rate modulation combined with the reflected longitudinal pressure waves (also having an azimuthal component) facing less resistance to reflect directly off an injection site due to the unchoked condition [30], provide a basis for opposing wave motion caused by a combination of continuous wave reflections and decoupling of the traveling detonations. This is consistent with the trends observed in detonation wave dynamics for increasing physical constriction for the $l_c = 76.1$ mm geometry, where counter-propagating behavior is more frequent and higher in severity, and lower wave speeds are observed. For the $l_c = 38.1$ mm case, it is possible that these wave reflections reach the fill zone at a period within the cycle that make it easier for the injectors to recover, or are of significantly lower amplitude because of a longitudinal resonance not being excited due to the shorter chamber length. Nevertheless, this analysis illustrates how high amplitude wave reflections at undesirable periods during the recovery time can drastically affect detonation propagation.

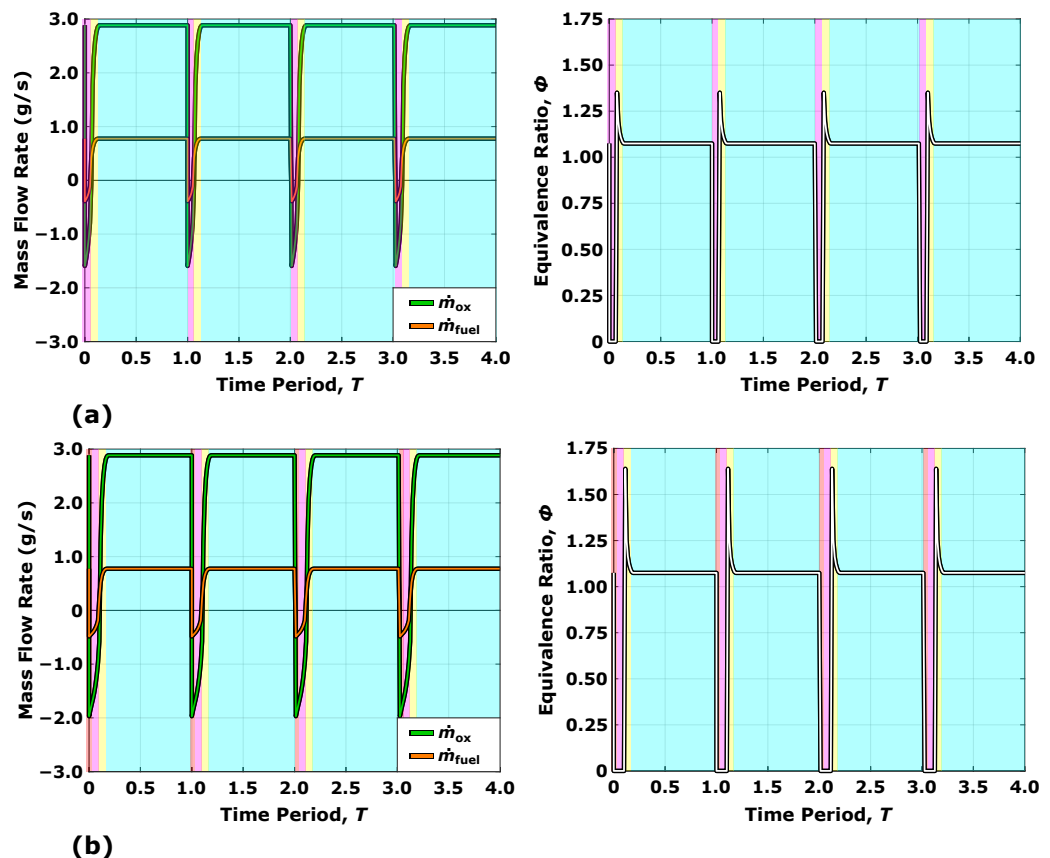


Figure 22. Temporal histories for the fuel and oxidizer mass flow rate (left) and corresponding equivalence ratio ϕ (right), for the (a) $p_{\text{rise}} = 20$ and (b) $p_{\text{rise}} = 30$ cases. Note that the cyan highlighted periods denote choked flow, yellow corresponds to unchoked flow, whereas red and magenta are reversed choked and unchoked flow, respectively.

5.1. Injection Recovery: Modeling and Simulation

In order to further illustrate the injection recovery process and its impact on the chamber wave dynamics, high-fidelity large-eddy simulations (LES) of the RDRE geometry have been performed using AHFM (ALREST High-Fidelity Modeling). The AHFM code is an extension of the Large Eddy Simulation with Linear Eddy (LESLIE) code [31], which has

been previously validated for a number of turbulent combustion applications, including highly oscillatory flow fields with combustion instabilities and detonations [32–36]. These fully three-dimensional simulations incorporate second-order McCormack schemes to advance the full reactive Navier–Stokes equations both temporally and spatially. Reaction chemistry is modeled using the FFCMy-12 mechanism, a 12 species/38 reaction reduced methane-oxygen mechanism tuned for high pressure combustion.

The complexity of RDRE physics creates challenges to comprehensively validate every scalar field tracked by the simulation. Nevertheless, this AHFM setup has previously been shown to adequately predict chamber pressures and detonation mode parameters such as the numbers of detonation waves and wave speeds for a variety of flow conditions compared to experiments [37,38]. However, it should be noted the code does exhibit the standard simulation overprediction of engine performance metrics, such as thrust and specific impulse [37,38]. The two simulations used for the current analysis are also the subject of another recent study [39], which focuses on experimental comparison and further simulation validation for these specific cases.

The simulated domain follows the experiment reported above, including distinct reactant manifolds, 72 discrete injector pairs, the combustion chamber, and an outflow plenum extending several chamber lengths downstream of the engine exhaust. Of these, the critical region of interest is the mixing zone, fully encompassing the injector plumes and the traveling detonations. Grid spacing in this annular region ranges from 50 to 60 μm , relaxing to approximately 300 μm further downstream. This yields a total cell count of 140 M hexahedrals within AHFM's block-structured system. While the spacing under-resolves boundary-layer effects, it does ensure the idealized one-dimensional length of the induction zone behind the leading shock wave is sufficiently resolved with 4–5 points. Additionally, due to the non-premixedness of the reactants in the RDRE, this critical detonation length-scale is further broadened [40]. These specific meshes have been adequately assessed in a prior work [39], and are consistent with other similar numerical studies [41,42].

Simulations for two full-length ($l_c = 76.2$ mm) chamber geometries are performed, one matching the most constricted nozzle configuration ($\epsilon_c = 2.40$), and the other matching the straight annulus. These two geometries are selected to show the differences between the injection recovery process between both corotating detonation mode propagation (i.e., corresponding to the unconstricted straight annulus) and counter-propagating behavior (i.e., $\epsilon_c = 2.40$ nozzle geometry). Flow conditions for both geometries are set to match cases at the intersection of the test matrix cross (Figure 3), corresponding to a total mass flow rate of 0.27 kg/s and equivalence ratio of $\phi = 1.1$.

One benefit of these large-eddy simulations is their ability to develop the steady-state wave dynamics of a detonation mode naturally, without any imposition of the number of waves. Both cases are initialized with the same type of high pressure and temperature detonation kernel, which temporarily causes a large number of detonation waves to propagate around the chamber in both directions. These waves then undergo an unsteady cascade process, characterized by a continuous change in number of waves and their wave speeds, before reaching a steady mode. Numerical convergence of the simulation is achieved when all the waves in the domain undergo a complete revolution of the chamber without a significant change in velocity once the target reactant flow rates are reached globally throughout the test article. Although this convergence criterion does not show that there are absolutely no long-scale transients left in the domain, it does ensure the engine reaches an operating mode that is stable over a complete operating period.

The end of the cascade process appears in Figure 23 for both the constricted ($\epsilon_c = 2.40$) and unconstricted geometries, showing azimuthal pressure integrated up to 1.5 cm above the injection plane to generate a similar temporal evolution of the chamber wave dynamics analogous to the integrated pixel intensities in Figure 10 (see Lietz et al. [37] for more information detailing the method used to generate these pressures from the simulation data). Note that in Figure 23a there are six discernible detonation structures at the beginning

of the window, starting at 1.0 ms from the simulation initialization. Over the following 0.5 ms, the detonations exhibit a wide range of velocities (denoted by the nonlinear slopes of the pressure fronts), measuring from 1020 to 2000 m/s, which eventually stabilize by 1.63 ms from the simulation start (denoted by the linear slopes of the pressure fronts). After this time, the three remaining waves continue traveling between 1620 m/s and 1650 m/s. Similarly, the $\epsilon_c = 2.40$ simulation shown in Figure 23b stabilizes by 1.55 ms from simulation start.

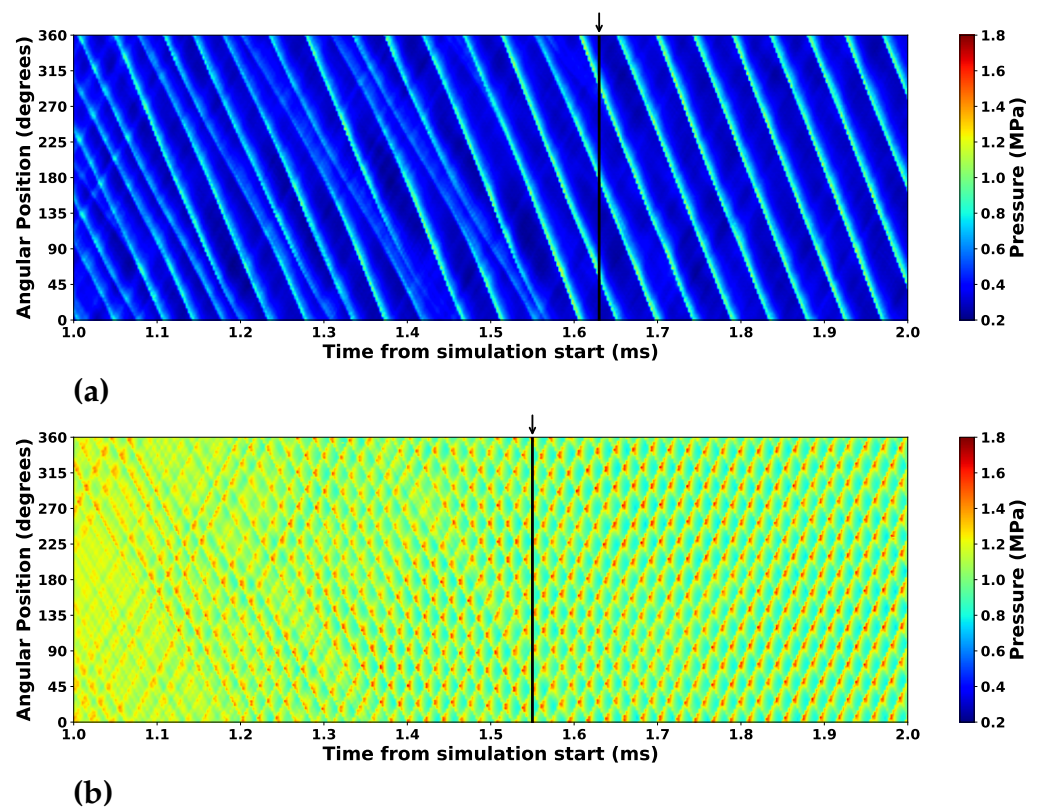


Figure 23. Detonation-region pressures for LES of (a) an unconstricted engine and (b) an engine with a nozzle constriction ($\epsilon_c = 2.40$); both engines operate at $\dot{m} = 0.27$ kg/s and $\phi = 1.1$. The time window demonstrates the transition to a steady operation condition, with arrows and vertical lines indicating when the engine is considered to have reached a steady operating mode: $t = 1.63$ ms for the straight chamber geometry, and $t = 1.55$ ms for the constricted chamber.

Results from these two simulations produce three corotating detonation waves for the straight annular geometry, and similar to the experiments, counter-propagating behavior for the $\epsilon_c = 2.40$ nozzle consisting of eight waves in both the clockwise and counterclockwise directions. Corresponding temporal histories of the oscillatory pressure within the detonation zone local to the injection plane for these simulations (see Figure 24a) show two distinct operating modes. In the case of the three-wave corotating mode (Figure 24a (left)), this pressure trace has a similar steep-fronted shape to the synthetic data generated for the injection recovery analysis (Figure 20). For the counter-propagating mode (Figure 24a (right)), the resultant oscillatory pressure, while periodic with steep-fronted waves, has an increased rate of pressure spikes with much higher variance compared to the corotating mode.

Accompanying injection properties are created by spatially integrating the flow fields over the injector orifices. Combined, the injection mass flow rates, the resultant local equivalence ratio and Mach numbers detail the injection recovery processes for the corotating and counter-propagating cases, as shown in Figure 24b–d, respectively. For the straight annulus case (Figure 24b–d (left)), the injection response is very similar to the predicted synthetic data analysis (Figure 21b,d), which show periodic unchoking in both injectors

without any flow reversal present prior to the injectors returning to their designed choked operation. This provides supporting evidence that the periodic unchoking process detailed in the injector recovery analysis can indeed cause non-uniformity in the reactant fill zone depending on the recovery symmetry between the fuel and oxidizer streams, as well as the ability of higher amplitude modulation due to wave reflections local to the injection plane.

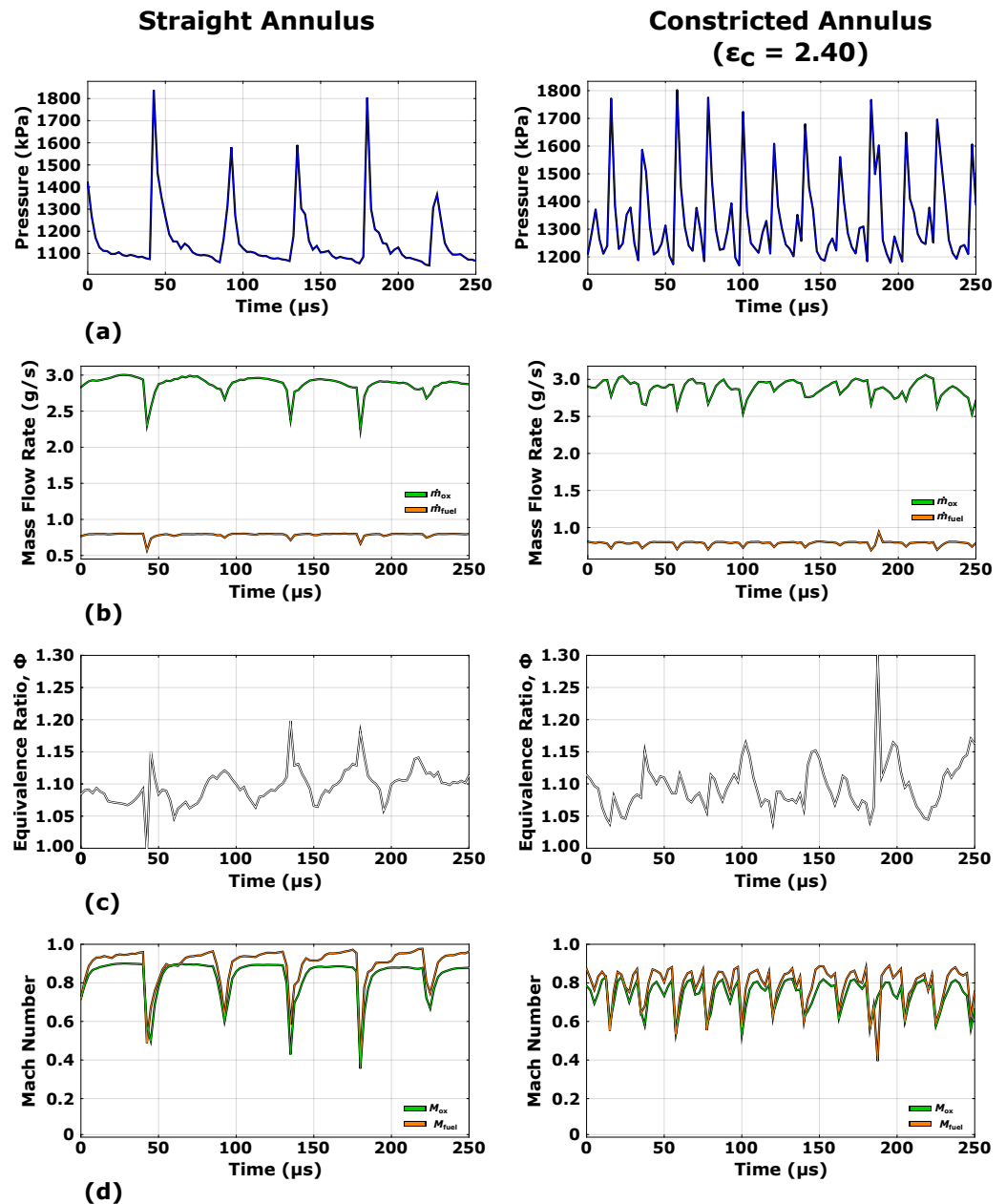


Figure 24. Injection recovery results from high-fidelity simulations for the straight (left) and $\epsilon_c = 2.40$ constricted annuli (right), showing the oscillatory (a) detonation pressure, (b) injection mass flow rate, (c) local equivalence ratio, and (d) injection Mach number.

For the constricted annular geometry, there is a different recovery process due to the counter-propagating behavior (Figure 24b–d (right)). Interestingly, as there is a large decrease in time between wave arrival events, the injectors are not able to return to choked operating conditions. This effect is further heightened due to the reduced injection pressure drop for the constricted geometry due to the increased chamber pressure caused by the physical throat addition. This is illustrated in the fuel and oxidizer injection Mach numbers for the constricted geometry (Figure 24d (right)), which show lower overall

averages compared to the straight annulus case. This lack of a choked regime during counter-propagating operation is likely what allows the counter-rotating detonations to pass through one another. Specifically, the injector response prevents any injector pair from injecting at the intended equivalence ratio (i.e., striating the reactant fill zone), and as a consequence, it becomes possible for a detonation to pass through a region without fully combusting the reactants. It is the existence of unburnt reactants which allows another detonation, traveling in the opposite direction, to continue propagating instead of encountering a region consisting entirely of spent propellant. This suggests that a core component of the mechanism sustaining counter-propagating behavior in constricted RDREs is an interaction between the constriction and the injectors.

6. Conclusions

Hot-fire test results for a 76.1 mm diameter modular rotating detonation rocket engine with various convergent nozzle designs are summarized for flow conditions ranging from equivalence ratio $\phi = 0.5$ – 2.5 and $\dot{m}_{\text{tot}} = 0.091$ – 0.680 kg/s. Three full-length annular convergent nozzle geometries with $l_c = 76.1$ mm at contraction ratios $\epsilon_c = 1.23$, 1.62 and 2.40 are investigated in this study. In general, engine performance increases linearly with increasing throat constriction for a given flow condition, which exhibit an overall increase of 8%, 16% and 27% for the $\epsilon_c = 1.23$, 1.62 and 2.40 nozzles, respectively, compared to the straight $\epsilon_c = 1.00$ geometry. However, the measured thrust compared to the ideal thrust for an equivalent constant-pressure engine ranges from $F/F_{\text{th}} = 80$ – 95% and does not increase appreciably with an increasing ϵ_c nozzle. Measured detonation wave speeds compared to the ideal Chapman-Jouguet values range from $U_{\text{wv}}/U_{\text{CJ}} = 50$ – 70% for the investigated flow conditions. From $\phi = 0.5$ – 2.5 , U_{wv} follows a similar trend to performance, with the highest wave speeds observed at $\phi \approx 1.5$. For $\dot{m}_{\text{tot}} = 0.091$ – 0.680 kg/s, wave speeds are generally insensitive to increasing flow rate and are mostly constant throughout. However, there is a greater presence of counter-propagating phenomenon with increasing ϵ_c at a given flow condition. This is accompanied by an increase in the number of waves m , as well as a decrease in the average wave speed. This may be a reason why there is not a notable performance increase compared to theoretical values for the more constricted convergent nozzle geometries.

In addition to the tests with the full-length annular nozzle, two reduced length geometries with $l_c = 38.1$ mm are also investigated (straight annulus and $\epsilon_c = 2.40$ nozzle). In general, there is no reduction in either operability or performance for the two shortened geometries across the entirety of the flow condition matrix. In fact, the $l_c = 38.1$ mm, $\epsilon_c = 2.40$ configuration actually exhibits a 6% increase in thrust and specific impulse, compared to the $l_c = 38.1$ mm cases, near the peak performance range of equivalence ratio at $\phi = 1.15$. This is also evident in the ideal thrust comparison for the shortened geometries, which again shows a maximum across all equivalence ratio conditions for the shortened $\epsilon_c = 2.40$ nozzle. Regarding the modal properties, the wave speeds associated with the active detonation modes for the $l_c = 38.1$ mm straight annulus are typically the same or higher than for the full-length straight annulus geometry, where a maximum $U_{\text{wv}}/U_{\text{CJ}} \approx 70$ – 75% is observed.

For the short constricted nozzle design, there is significantly less prevalent counter-propagating behavior throughout the various flow conditions than is observed for the full-length nozzle configuration. This is likely due to the location of the physical throat being shifted towards the injection plane for the shortened geometry, which may alter the detonation-injection coupling. In summary, this work serves to elucidate the influence of annular length and exit constriction on RDRE operation and performance. The trends identified should serve as a foundation for future studies to optimally expand the oscillatory exit flows through these devices, and thus optimize their performance.

Author Contributions: Conceptualization, J.W.B., W.A.H.J., S.A.D. and R.D.S.; methodology, J.W.B., B.R.B., M.C.R. and R.D.S.; software, J.W.B., B.R.B. and M.C.R.; formal analysis, J.W.B., B.R.B. and M.C.R.; investigation, J.W.B., B.R.B. and S.A.D.; writing—original draft preparation, J.W.B. and M.C.R.; writing—review and editing, J.W.B., B.R.B., M.C.R., S.A.D., W.A.H.J. and R.D.S.; supervision, J.W.B., W.A.H.J. and R.D.S.; funding acquisition, J.W.B. and W.A.H.J. All authors have read and agreed to the published version of the manuscript.

Funding: This work has been supported by the Air Force Office of Scientific Research (AFOSR) under AFRL Lab Task 20RQCOR63 funded by the AFOSR Energy, Combustion, Non-Equilibrium Thermodynamics portfolio with Chiping Li as program manager.

Acknowledgments: The authors would like to thank the Air Force Research Laboratory EC-1 test crew for their assistance during testing for this study.

Conflicts of Interest: The authors declare no conflict of interest. The funders had no role in the design of the study; in the collection, analyses, or interpretation of data; in the writing of the manuscript, or in the decision to publish the results.

References

1. Bykovskii, F.; Zhdan, S.; Vedernikov, E.F. Continuous Spin Detonations. *J. Propuls. Power* **2006**, *22*, 1204–1216. [[CrossRef](#)]
2. Smith, R.D.; Stanley, S.B. Experimental Investigation of Rotating Detonation Rocket Engines for Space Propulsion. *J. Propuls. Power* **2021**, 1–11. [[CrossRef](#)]
3. Frolov, S.M.; Aksenov, V.S.; Ivanov, V.S.; Medvedev, S.N.; Shamshin, I.O. Flow Structure in Rotating Detonation Engine with Separate Supply of Fuel and Oxidizer: Experiment and CFD. In *Shock Wave and High Pressure Phenomena*; Springer International Publishing: Cham, Switzerland, 2017; pp. 39–59. [[CrossRef](#)]
4. Stechmann, D.P.; Heister, S.D.; Sardeshmukh, S.V. High-Pressure Rotating Detonation Engine Testing and Flameholding Analysis with Hydrogen and Natural Gas. In Proceedings of the 55th AIAA Aerospace Sciences Meeting, Grapevine, TX, USA, 9–13 January 2017. [[CrossRef](#)]
5. Bennewitz, J.; Bigler, B.; Hargus, W.; Danczyk, S.; Smith, R. Characterization of Detonation Wave Propagation in a Rotating Detonation Rocket Engine using Direct High-Speed Imaging. In Proceedings of the 54th AIAA Joint Propulsion Conference, Cincinnati, OH, USA, 9–11 July 2018.
6. Goto, K.; Nishimura, J.; Higashi, J.; Taki, H.; Ukai, T.; Hayamizu, Y.; Yamada, T.; Watanabe, S.; Hotta, K.; Inakawa, T.; et al. Preliminary Experiments on Rotating Detonation Rocket Engine for Flight Demonstration Using Sounding Rocket. In Proceedings of the 2018 AIAA Aerospace Sciences Meeting, Kissimmee, FL, USA, 8–12 January 2018. [[CrossRef](#)]
7. Frolov, S.M.; Aksenov, V.S.; Ivanov, V.S.; Medvedev, S.N.; Shamshin, I.O.; Yakovlev, N.N.; Kostenko, I.I. Rocket Engine with Continuous Detonation Combustion of the Natural Gas–Oxygen Propellant System. *Dokl. Phys. Chem.* **2018**, *478*, 31–34. [[CrossRef](#)]
8. Bykovskii, F.A.; Zhdan, S.A.; Vedernikov, E.F. Continuous Detonation of the Liquid Kerosene–Air Mixture with Addition of Hydrogen or Syngas. *Combust. Explos. Shock Waves* **2019**, *55*, 589–598. [[CrossRef](#)]
9. Paxson, D.E.; Schwer, D.A. Operational Stability Limits in Rotating Detonation Engine Numerical Simulations. In Proceedings of the AIAA Scitech 2019 Forum, San Diego, CA, USA, 7–11 January 2019. [[CrossRef](#)]
10. Goto, K.; Nishimura, J.; Kawasaki, A.; Matsuoka, K.; Kasahara, J.; Matsuo, A.; Funaki, I.; Nakata, D.; Uchiumi, M.; Higashino, K. Propulsive Performance and Heating Environment of Rotating Detonation Engine with Various Nozzles. *J. Propuls. Power* **2019**, *35*, 213–223. [[CrossRef](#)]
11. Bluemner, R.; Bohon, M.D.; Paschereit, C.O.; Gutmark, E.J. Effect of inlet and outlet boundary conditions on rotating detonation combustion. *Combust. Flame* **2020**, *216*, 300–315. [[CrossRef](#)]
12. Stechmann, D.P. Experimental Study of High-Pressure Rotating Detonation Combustion in Rocket Environments. Ph.D. Thesis, Purdue University, West Lafayette, IN, USA, 2017.
13. Bigler, B.R.; Bennewitz, J.W.; Schumaker, S.A.; Danczyk, S.A.; Hargus, W.A. Injector Alignment Study for Variable Mixing in Rotating Detonation Rocket Engines. In Proceedings of the AIAA Scitech 2019 Forum, San Diego, CA, USA, 7–11 January 2019. [[CrossRef](#)]
14. Bennewitz, J.W.; Bigler, B.R.; Pilgram, J.J.; Hargus, W.A. Modal Transitions in Rotating Detonation Rocket Engines. *Int. J. Energetic Mater. Chem. Propuls.* **2019**, *18*, 91–109. [[CrossRef](#)]
15. Smith, R.D.; Stanley, S.B. Experimental Investigation of Continuous Detonation Rocket Engines for In-Space Propulsion. In Proceedings of the 52nd AIAA/SAE/ASEE Joint Propulsion Conference, Salt Lake City, UT, USA, 25–27 July 2016.
16. Stevens, C.; Fotia, M.; Hoke, J.; Schauer, F. Comparison of Transient Response of Pressure Measurement Techniques with Application to Detonation Waves. In Proceedings of the 53rd AIAA Aerospace Sciences Meeting, Kissimmee, FL, USA, 5–9 January 2015.
17. Lightfoot, M.D.; Danczyk, S.A.; Watts, J.M.; Schumaker, S.A. *Accuracy and Best Practices for Small-Scale Rocket Engine Testing*; Technical Report; AFRL-RZ-ED-TP-2011-420; Air Force Research Laboratory Wright-Patterson AFB: Dayton, OH, USA, 2011.

18. Taylor, J.R. *An Introduction to Error Analysis: The Study of Uncertainties in Physical Measurements*, 2nd ed.; University Science Books: Sausalito, CA, USA, 1997.
19. Beckwith, T.G.; Roy D.M.; Lienhard, J.H. *Mechanical Measurements*, 6th ed.; Pearson Prentice Hall: Upper Saddle River, NJ, USA, 2007.
20. Gordon, S.; McBride, B.J. *Computer Program for Calculation of Complex Chemical Equilibrium Compositions and Applications, Part I: Analysis*; Technical Report NASA RP-1311; National Aeronautics and Space Administration, Lewis Research Center: Cleveland, OH, USA, 1994.
21. Sutton, G.P.; Biblarz, O. *Rocket Propulsion Elements*, 8th ed.; John Wiley & Sons, Inc.: Hoboken, NJ, USA, 2010.
22. Bennewitz, J.; Bigler, B.; Schumaker, S.; Hargus, W. Automated Image Processing Method to Quantify Rotating Detonation Wave Behavior. *Rev. Sci. Instrum.* **2019**, *90*. [[CrossRef](#)] [[PubMed](#)]
23. Wolanski, P. Rotating Detonation Wave Stability. In Proceedings of the 23rd International Colloquium For Dynamics of Explosions and Reactive Systems, Irvine, CA, USA, 24–29 July 2011.
24. Chapman, D. On the Rate of Explosion in Gases. *Lond. Edinb. Dublin Philos. Mag. J. Sci.* **1899**, *47*, 90–104. [[CrossRef](#)]
25. Lietz, C.; Desai, Y.; Munipalli, R.; Schumaker, S.A.; Sankaran, V. Flowfield analysis of a 3D simulation of a rotating detonation rocket engine. In Proceedings of the AIAA Scitech 2019 Forum, San Diego, CA, USA, 7–11 January 2019. [[CrossRef](#)]
26. Bykovskii, F.A.; Zhdan, S.A. Current status of research of continuous detonation in fuel–air mixtures (Review). *Combust. Explos. Shock Waves* **2015**, *51*, 21–35. [[CrossRef](#)]
27. Kayser, J.C.; Shambaugh, R.L. Discharge coefficients for compressible flow through small-diameter orifices and convergent nozzles. *Chem. Eng. Sci.* **1991**, *46*, 1697–1711. [[CrossRef](#)]
28. EPA. *Risk Management Program Guidance for Offsite Consequence Analysis*; Technical Report EPA 550-B-99-009; Chemical Emergency Preparedness and Prevention Office: Washington, DC, USA, 1999.
29. Zucrow, M.J.; Hoffman, J.D. *Gas Dynamics: Volume 1*; John Wiley & Sons, Inc.: Hoboken, NJ, USA, 1976.
30. Redhal, S.C.; Burr, J.R.; Yu, K.H. Fuel Injection Dynamics and Detonation Wave Interaction in Rectangular Channel. In Proceedings of the AIAA Scitech 2019 Forum, San Diego, CA, USA, 7–11 January 2019. [[CrossRef](#)]
31. Kim, W.W.; Menon, S. An unsteady incompressible Navier–Stokes solver for large eddy simulation of turbulent flows. *Int. J. Numer. Methods Fluids* **1999**, *31*, 983–1017. [[CrossRef](#)]
32. Génin, F.; Menon, S. Studies of shock/turbulent shear layer interaction using Large-Eddy Simulation. *Comput. Fluids* **2010**, *39*, 800–819. [[CrossRef](#)]
33. Masquelet, M.; Menon, S. Large-Eddy Simulation of Flame-Turbulence Interactions in a Shear Coaxial Injector. *J. Propuls. Power* **2010**, *26*, 924–935. [[CrossRef](#)]
34. Srinivasan, S.; Ranjan, R.; Menon, S. Flame Dynamics During Combustion Instability in a High-Pressure, Shear-Coaxial Injector Combustor. *Flow Turbul. Combust.* **2015**, *94*, 237–262. [[CrossRef](#)]
35. Gottiparthi, K.C.; Menon, S. A Study of Interaction of Clouds of Inert Particles with Detonation in Gases. *Combust. Sci. Technol.* **2012**, *184*, 406–433. [[CrossRef](#)]
36. Yang, S.; Ranjan, R.; Yang, V.; Sun, W.; Menon, S. Sensitivity of predictions to chemical kinetics models in a temporally evolving turbulent non-premixed flame. *Combust. Flame* **2017**, *183*, 224–241. [[CrossRef](#)]
37. Lietz, C.; Desai, Y.; Hargus, W.A.; Sankaran, V. Parametric investigation of rotating detonation rocket engines using large eddy simulations. In Proceedings of the AIAA Propulsion and Energy 2019 Forum, Indianapolis, IN, USA, 19–22 August 2019. [[CrossRef](#)]
38. Lietz, C.; Ross, M.; Desai, Y.; Hargus, W.A. Numerical investigation of operational performance in a methane-oxygen rotating detonation rocket engine. In Proceedings of the AIAA Scitech 2020 Forum, Orlando, FL, USA, 6–10 January 2020. [[CrossRef](#)]
39. Ross, M.; Lietz, C.; Desai, Y.; Hamilton, J.; Hargus, W. *Investigation into the Impact of an Exit Constriction on Rotating Detonation Rocket Engines, Using Large Eddy Simulations*; Technical Report AD1108842; Air Force Research Laboratory: Edwards, CA, USA, 2019.
40. Prakash, S.; Fiévet, R.; Raman, V.; Burr, J.; Yu, K.H. Analysis of the Detonation Wave Structure in a Linearized Rotating Detonation Engine. *AIAA J.* **2020**, *58*, 5063–5077. [[CrossRef](#)]
41. Pal, P.; Kumar, G.; Drennan, S.; Rankin, B.A.; Som, S. Numerical Modeling of Supersonic Combustion in a Non- Premixed Rotating Detonation Engine. In Proceedings of the 11th U.S. National Combustion Meeting, Pasadena, CA, USA, 24–27 March, 2019.
42. Schwer, D.; Kailasanath, K. Feedback into Mixture Plenums in Rotating Detonation Engines. In Proceedings of the 50th AIAA Aerospace Sciences Meeting Including the New Horizons Forum and Aerospace Exposition, Nashville, TN, USA, 9–12 January 2012. [[CrossRef](#)]